Title
Tunability of Aromatic Carbon Materials

Author
Wang, Chen

Publication Date
2018

UNIVERSITY OF CALIFORNIA,
IRVINE

Tunability of Aromatic Carbon Materials

DISSERTATION

submitted in partial satisfaction of the requirements
for the degree of

DOCTOR OF PHILOSOPHY

in Materials Science and Engineering

by

Chen Santillan Wang

Dissertation Committee:
Associate Professor Regina Ragan, Chair
Professor Ruqian Wu
Professor Peter Burke

2018

DEDICATION

To My Dad

…who still won’t think I appreciate him enough after reading this.

TABLE OF CONTENTS

Page

LIST OF FIGURES

LIST OF TABLES

ACKNOWLEDGMENTS

I would like to express my deep gratitude to my research mentors who have played a critical role in shaping the scientist I am today. I want to thank Professor Regina Ragan for welcoming me into her research group, providing the opportunity to participate in wide-ranging collaborations, and pushing me to explore exciting new problem spaces in materials science outside of my comfort zone. Similarly, I would also like to thank Professor Ludwig Bartels for introducing me to graduate research, surface science, and the promise of two-dimensional materials.

I am also grateful to my committee members, Professors Peter Burke and Ruqian Wu. I always felt welcome in both of their research groups to ask questions, borrow tools, and ponder the limits of new materials. Similarly, Professor Jeppe Vang Lauritsen also welcomed me into his lab during my research stay at Aarhus University and Signe Grønborg made me feel at home in research and Danish culture.

My labmates, both from UC Irvine and UC Riverside, have provided immeasurable support to me. Adrian Garcia endured late nights and weekends finishing sample preparations to ensure we could collect the necessary measurements. Robert Sanderson persevered with me to repair the scanning tunneling microscope and obtain beautiful nanoscale images. Everyone in the Ragan group, including William Thrift and Cuong Nguyen, provided me with sanity checks when needed. My Bartels group "labmigos" – including Velveth Klee, Ariana Nguyen, David Barroso, Joseph Martinez, Daniel Lu, Cindy Merida, Sahar Naghibi, and Gretel Von Son – always rejuvenated me, keeping research fun and silly. John Mann, Wenhao Lu, Quan Ma, and Dezheng Sun served as wonderful mentors for me in my early days as a graduate student. I would like to also thank Edwin Preciado for serving as my partner in crime through early mornings, late nights, and long drives.

In the next stage of my life, I am honored to be serving as the inaugural Jill Hruby Fellow at Sandia National Laboratories in Livermore, California. Such a tremendous opportunity would not be possible without the incredible support provided by my mentors Konrad Thürmer and Norman Bartelt, who continue to teach me how to rigorously approach science.

Finally, I would like to thank my friends and family. In addition to providing me their love and friendship, my childhood friends, Cynthia Chor and Anna Gruzman, edited countless essays, statements, and applications for me. My mother and my brother always reassured me that I was smart and capable, even when I did not feel that way about myself. Conversely, my father always pushed me critically evaluate and aspire to be a better version of myself. Both him and Phi Pham supported me enormously through the tumultuous journey of graduate school through every day, simple things like proofreading, phone calls, and sending cute bunny pictures.

This material is based upon work supported by the National Science Foundation Graduate Research Fellowship under Grant No. DGE-1321846 and DGE-1326120. This work was supported by the Sandia Laboratory Directed Research and Development Program. Sandia National Laboratories is a multimission laboratory managed and operated by National Technology and Engineering Solutions of Sandia LLC, a wholly owned subsidiary of Honeywell International Inc. for the U.S. Department of Energy's National Nuclear Security Administration under contract DE-NA0003525. In addition, this material is based upon work supported by the U.S. Department of Energy, Office of Science, Office of Workforce Development for Teachers and Scientists, Office of Science Graduate Student Research (SCGSR) program. The SCGSR program is administered by the Oak Ridge Institute for Science and Education (ORISE) for the DOE. ORISE is managed by ORAU under contract number DE-AC05-06OR23100. For computational simulations, this work used the Extreme Science and Engineering Discovery Environment (XSEDE), which is supported by National Science Foundation grant number ACI-1548562. The allocation accounts used in this research were CHE140084 and DMR150047.

CURRICULUM VITAE

Chen Santillan Wang

2011	B.S. in Electrical and Computer Engineering, Franklin W. Olin College of Engineering
2011 – 2014	Research Assistant, Ludwig Bartels Group University of California, Riverside
2013	Visiting Foreign Researcher, Jeppe Vang Lauritsen Group Aarhus University, Denmark
2014	M.S. in Materials Science and Engineering University of California, Riverside
2014 – 2018	Research Assistant, Regina Ragan Group University of California, Irvine
2017	Science Graduate Student Research Program Awardee Sandia National Laboratories, Livermore, CA
2018	Ph.D. in Materials Science and Engineering, University of California, Irvine

ABSTRACT OF THE DISSERTATION

Tunability and Evolution of Aromatic Carbon Materials

By

Chen Santillan Wang

Doctor of Philosophy in Materials Science and Engineering

University of California, Irvine, 2018

Associate Professor Regina Ragan, Chair

Carbon is both abundant and functionally versatile due to the variability of orbital hybridization of carbon atoms forming planar and tetrahedral bonds leading to many allotropes. Different allotropes exhibit different physical properties such as electrical conductivity, surface area, and surface chemistry. The work presented here focuses on aromatic carbon materials examining tunability of physical properties, molecular to macroscopic structural formation, and importance in environmental applications, specifically soot pollution mitigation and next-generation single atom catalysis.

First, scanning tunneling microscopy (STM) experiments explore the intermolecular interactions of coronene ($C_{12}H_{24}$), a polycyclic aromatic hydrocarbon hypothesized to play a key role in incipient soot formation. The hazardous impacts of incipient soot – including lengthy suspension in the earth's atmosphere and deep penetration into human respiratory systems – may be circumvented through an improved understanding of soot formation. Observations of coronene clusters reveal structures strikingly similar to recent models of clusters hypothesized to initiate soot formation. In contrast to mature soot, cluster surfaces

are composed primarily of molecular edges, suggesting that a critical step significantly transforming cluster geometry is necessary for soot evolution.

Second, a first principle approach is used to identify how the local molecular environment on a graphene support can be used to stabilize a single platinum atom catalyst. Inspired by visions of achieving ultimate cost-effectiveness and performance, a single atom catalyst represents the most efficient use of precious metals while concurrently offering the potential for high chemical activity. Density functional theory results indicate that pyridinic N-doped graphene is a promising candidate to support a single Pt atom acting as a catalyst that is resistant to poisoning and enhances CO oxidation efficiency. Experimental efforts demonstrate a pathway towards developing these supports, using bicontinuous interfacially jammed emulsion gels as templates for the growth of three-dimensional, porous graphene. STM, X-ray photoelectron spectroscopy, and Raman spectroscopy characterize the resultant architectures, relating nanoscale observations to macroscale properties such as specific surface area and mechanical strength.

This work, examining aromatic carbon materials, demonstrates how surface science techniques can unravel self-assembly and untapped potential of nanoscale materials and the physics that shape our macroscale environment.

CHAPTER 1: INTRODUCTION

1.1 Aromatic Carbon – The Stuff of Human Past, Present, and Future

Most organic species are composed of carbon, and throughout its history, mankind has sought to manipulate this special element. In about 5000 BC, early humans began using carbon as an energy producing material in the form of charcoal to heat and cook. Later, humans used carbon as a chemical material in the form of coal to smelt copper and iron.[1] Even in present times, carbon still plays an important role in society; indeed, for this reason, there exists a field of science primarily focused on studying carbon-based. Organic chemistry involves study of the structure, properties, and reactions of organic materials, and is, primarily, focused on carbon compounds.[2] Without such exploration, everyday items would not exist – including, but not limited to plastics, cloths, drugs, preservatives, and many sources of fuel.[3]

The work presented here focuses its scope on carbon that adopts an "aromatic structure", where aromaticity is defined by four main characteristics:

1. A delocalized conjugated π system, most commonly an arrangement of alternating single and double bonds.
2. Coplanar structure, with all the contributing atoms in the same plane.
3. Contributing atoms arranged in one or more rings.
4. Conformation to Hückel's rule, which requires that a number of π delocalized electrons equal to $4n + 2$ π, where $n = 0, 1, 2, 3$, and so on.

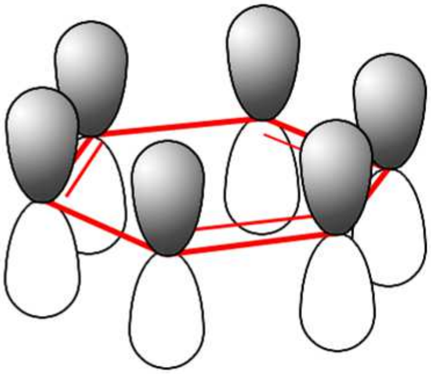

Figure 1: A representation the circular π-bond that defines aromaticity. The electron density is evenly distributed through a π-bond above and below the ring.

Typically, aromatic carbon species are terminated by hydrogen atoms at the outer perimeter of the molecule and, consequently, are referred to as polyaromatic hydrocarbons (PAHs). Earlier discussion was devoted to summarizing the role of carbon in human history. However, even before the existence of humans, PAHs have been speculated as the building blocks of original life. More than 20% of the carbon in the universe is estimated to exist as some form of PAH, and these species seem to have formed abundantly at the early stages of the universe, roughly 2 billion years after the Big Bang. [4,5] Additionally, PAHs are the most prolific of the known polyatomic molecules in the visible universe, and are considered constituents of the primordial sea.[6] For this reason, some theories speculate that PAHs played a major role facilitating the origin of life by mediating the synthesis of RNA molecules.[7,8]

However, aromatic carbon is not simply an important figure of the past; it is a material with incredible promise to shape future technology. In 2004, the discovery of the two-dimensional allotrope of carbon – graphene – kickstarted a revolution to study the properties of the novel, new material and to develop applications for it.

1.2 Graphene

Graphene is an atomically thin material composed of pure carbon, which forms a honeycomb lattice composed of aromatic rings, which in theory extends infinitely. Because of its unique crystal structure, graphene exhibits many novel properties.

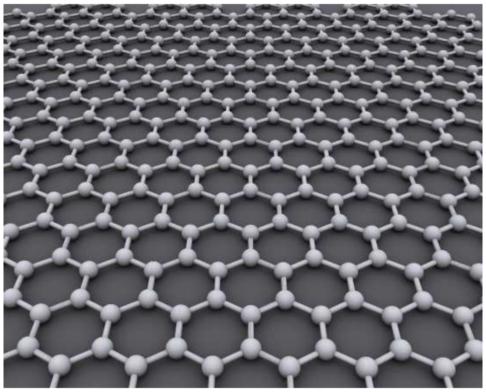

Figure 2: Honeycomb carbon lattice of graphene, which is constrained to and extends infinitely in two dimensions.

Graphene's properties were theoretically predicted in the mid-1900s by Wallace through tight-binding calculations.[9] Early research identified many of graphene's novel properties such as its zero bandgap; however, progress was hampered by the prevailing misconception that two-dimensional metals were too unstable and consequently unsuitable for practical applications.[10] Monolayer graphene was first isolated from bulk graphite by Andre Geim and Konstantin Novoselov. Using mechanical exfoliation, sometimes referred to as "scotch-tape method", the two scientists separated layers of bulk graphite by repeated peeling, eventually thinning multi-layer graphene to single layer.[11] After this achievement, commercial and scientific interest in graphene surged as researchers endeavored to take advantage of its numerous unique properties, including its high electron mobility at room-temperature, high thermal conductivity, extremely high tensile strength, and near impermeability. Geim and Novoselov would go on to win the

Nobel Prize in Physics in 2010 “for groundbreaking experiments regarding the two-dimensional material graphene”.[12] Nowadays, graphene is heavily researched, and many advancements have been made in developing applications for lightweight materials, nanoelectronics, energy storage, chemical filtering, and more.[11,13–20]

1.3 Thesis Overview

The work presented in this thesis explores aromatic carbon materials, their tunability, and their evolution into larger structures via surface science characterization – primarily, scanning tunneling microscopy (STM) and density functional theory (DFT).

The first portion of this thesis (chapter 4) explores coronene, a polyaromatic hydrocarbon with the molecular formula $C_{12}H_{24}$ and one of the primary precursors of incipient soot. This work is motivated by the goal of mitigating the formation of soot, whose hazardous impacts include damaging the earth’s atmosphere and causing various human respiratory illnesses. STM observations of coronene clusters reveal structures that resemble those predicted by recently developed models simulating incipient soot formation. In contrast to mature soot, the surfaces of these clusters are predominantly composed of molecular edges, suggesting that passivating these edges may offer a means of inhibiting the growth of particles. These findings have transformative impact on the current understanding of soot and proposes a new paradigm for developing technologies mitigating soot pollution.

The second portion of this thesis focuses on the development of aromatic carbon-based catalytic supports. DFT calculations are used to predict catalytic enhancement of graphene via impregnation of platinum nanoclusters (chapter 5). To bring these predictions to life, bicontinuous interfacially jammed emulsion gels (bijels) are implemented as templates for graphene architectures (chapter 6). By characterizing the growth mechanics of graphene on the template material, nanoscale observations are related to macroscale properties for ideal catalytic supports such as high urface area and mechanical strength.

CHAPTER 2: Experimental Methods

2.1 Scanning Tunneling Microscopy

In 1981, Gerd Binnig and Heinrich Rohrer created the first STM at the IBM Zurich Research Laboratory,[21–23] revolutionizing the field of surface science by providing images with three-dimensional, real-space information and extremely high spatial resolution. With this invention, they resolved atomic steps and surface reconstructions of Au and $CaIrSn_4$ (110) surfaces as well as determined the first real space configuration of the Si(111) (7x7) reconstruction.[24,25] In recognition of their achievements, Binnig and Rohrer won the Nobel Prize in Physics in 1986.[26] Since then, scanning probe microscopy (SPM) has grown into its own field. SPM is generally defined as a visualization technique in which a sharp probe scans across a surface to detect specific physical information and map it out with high resolution. Atomic force microscopy (AFM) is one of the most popular offshoots of SPM and uses a cantilever probe to measure short-range repulsive interactions between the tip and the sample. However, depending on the implementation of the probe, SPM may measure and manipulate an array of different properties such as surface potential (KPFM), capacitance (SCM), and magnetic force (MFM). Even so, because of its ability to obtain detailed local atomic-scale information from surfaces, STM remains a staple tool in surface science to interrogate materials and physics at the atomic scale.

2.1.1 Working Principles of a Scanning Tunneling Microscope

In classical mechanics, an electron cannot penetrate a potential barrier with an energy higher than its own. However, in quantum mechanics, when a sharp metal tip is brought within close proximity (~5 Å) of a conducting surface, the electronic wave functions of the tip and surface will begin to overlap. As a result, a phenomenon referred to as "tunneling" will occur; the tip and surface will exchange electrons through the classically forbidden vacuum gap. Upon applying a small bias voltage, V_G, between the tip and the surface, a net flow of electrons will travel from filled states on the surface into empty states of the tip (or vice versa depending on the polarity of V_G). This effect is measurable as a current, I_T, and strongly depends on the size of the vacuum gap due to the exponential decay of the electronic wave functions. STM takes advantage of this effect that is incredibly sensitive to separation distance and uses tunneling as a mechanism to gather electronic information on a surface and produce feedback such that the tip may adjust to surface topography.

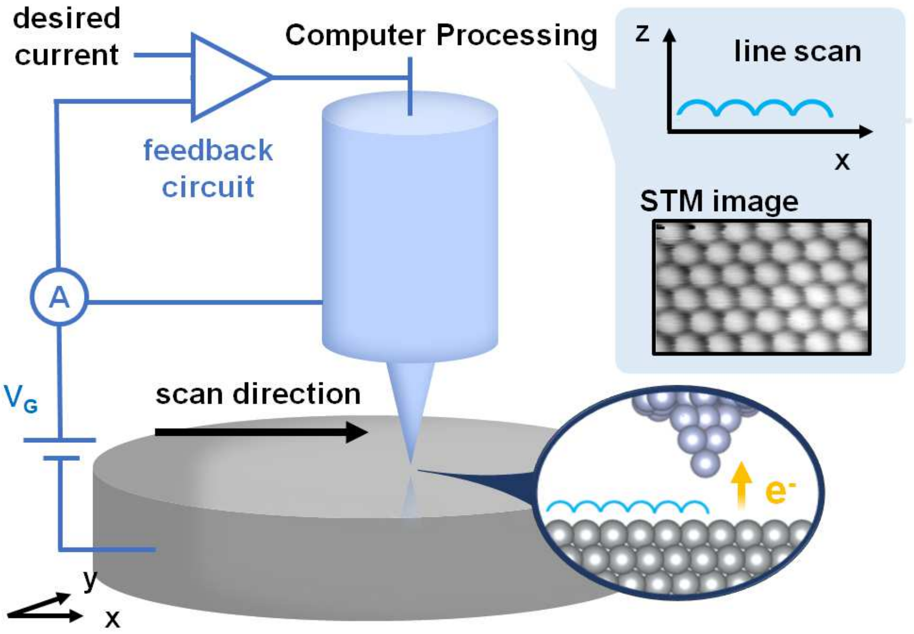

Figure 3: Schematic of the operating principles of an STM. The circular inset illustrates the tunneling effect that occurs during a single line scan. The rectangular inset illustrates how the computer processed this line scan and build an image from multiple line scans.

2.1.2 A Simple One-Dimensional Model

To understand the mechanism in greater detail, it is helpful to consider a simple one-dimensional model with two systems, a sample with work function ϕ_s and a probe with work function ϕ_p. Between the two, there is vacuum gap of D with a constant potential barrier U. In the region 0 < d < D and the wave function ψ(d) describes an electron with energy ε < U that is moving in the positive D direction:

$$\psi(d) = \psi(0)e^{-\kappa d}, \text{where } \kappa = \frac{\sqrt{2m_e(U-E)}}{\hbar}$$

The probability P of observing an electron at the other side of the potential barrier, where d=D, is proportional to the square of the wave function such that:

$$P \sim |\psi(D)|^2 = |\psi(0)|^2 e^{-2\kappa D}$$

If $eV_G \ll \phi$, then $U - E$ may be approximated as ϕ and the probability that an electron in the nth state of the sample with energy E_n, where $E_F < E_n < E_F - eV_G$, will tunnel to an empty state in the probe becomes:

$$P \sim |\psi(D)|^2 = |\psi(0)|^2 e^{-\frac{2}{\hbar}\sqrt{2m_e\phi D}}, \text{where } \phi = \frac{\phi_s+\phi_p}{2}$$

The tunneling current I_t is directly proportional to the total number of sample states within the energy interval eV_G:

$$I_t \sim \sum_{E_n = E_F - eV_G}^{E_F} \left|\psi_{n(D)}\right|^2$$

If the density of the electronics states does not vary significantly within the interval from $E_F - eV_G$ to E_F , then the current reflects the local density of states of the sample at the Fermi level and at the position of the tip:

$$I_t \sim V_G \rho_s(d = D, E_F) = V_G \rho_s(0, E_F) e^{-\frac{2}{\hbar}\sqrt{2m_e\phi D}}$$

Tersoff-Hamann theory more rigorously arrives at a similar result.

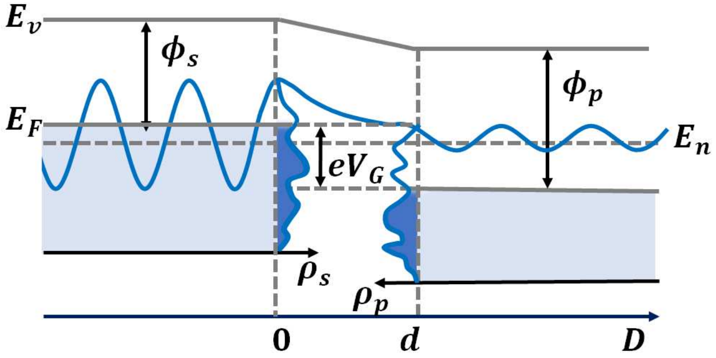

Figure 4: Schematic illustrating the energy level diagrams for sample-probe tunnel junction. V_G represents the gap voltage applied to the sample relative to the probe. ϕ_s and ϕ_p are the work functions of the sample and probe, respectively. Similarly, ρ_s and ρ_p represent the density of states. Tunneling only occurs within the small energy interval eV_G. E_n represents a wave function with energy "n that decays exponentially in the junction but still has a non-zero amplitude at the position of the probe tip. These are all drawn with respect to the vacuum energy E_v and the Fermi energy of the sample E_F.

2.1.3 Tersoff-Hamann Theory

The Tersoff-Hamann model[27] provides a conceptually simple framework for interpreting STM images and is the most widely used model in the field. Using the formalism introduced by Bardeen,[28] it treats the probe and surface as two non-interaction systems and solves the stationary Schrodinger equation to obtain the wave functions each. [28,29] Tunneling current can then be calculated via time-dependent perturbation theory.

Derived from first-order time-dependent perturbation theory, Fermi's golden rule states that the transition rate for an electron to tunnel from an initial state (sample) to a final state (probe) is given by the equation:

$$R_{s\to p} = \frac{2\pi}{\hbar}\,|M|^2\delta(E\psi_s - E\psi_p)$$

(Only tunneling, where electrons elastic move between same energy states is considered, as indicated by the delta function.) Bardeen showed that the tunneling matrix element, M, can be expressed as:

$$M = \frac{\hbar}{2m}\int_{S_0}\left(\psi_s^*\nabla\psi_\mathrm{p} - \psi_p\nabla\psi_s^*\right)d\vec{S}$$

The integration takes place over any surface within the tunneling gap (S_0). Referring back to Fermi's golden rule, assuming a negative bias voltage such that tunneling occurs from sample to tip, and accounting for electron spin, the tunneling current may be expressed as:

$$I_{s\to p} = \frac{4\pi e}{\hbar}\int_{-\infty}^{\infty} n_s(E)f(E)|M|^2 n_p(E + eV_G)[1 - f(E + eV_G)]dE$$

n_s and n_p are the density of states (DOS) of the sample and probe, respectively. $f(E)$ represents the Fermi distribution and is fully expressed as:

$$f(E) = \left[1 + exp\frac{E - E_F}{k_B T}\right]^{-1}$$

In accordance with the Pauli exclusion principle, tunneling will only occur from filled states into empty states. Tunneling current will predominantly flow from the sample to the probe; however, a smaller current will flow in the opposite direction, such that the total current flow will be:

$$I = I_{s\to p} - I_{p\to s} = \frac{4\pi e}{\hbar}\int_{-\infty}^{\infty}|M|^2 n_s(E)n_p(E + eV_G)[f(E) - f(E + eV_G)]dE$$

As a low enough temperature, the Fermi distribution may be described by a simple step function, thus simplifying the equation to:

$$I \approx \frac{4\pi e}{\hbar}\int_{E_F - eV_G}^{E_F}|M|^2 n_s(E)n_p(E + eV_G)]dE$$

If the matrix element remains relatively constant with respect to energy, it can be separated out from the equation such that tunneling current becomes expressed as a simple convolution of the surface and probe DOS. By assuming a simple s-wave model for a probe with spherically symmetric wave functions centered at the center of curvature of a fine tip $\overrightarrow{r_0}$, the tunneling current equation can be further simplified to:

$$I \sim V_G \sum_s |\psi_s(\overrightarrow{r_0})|^2 \delta(E_s - E_F) = V_G \rho(E_F, \overrightarrow{r_0})$$

The sum extends over sample states evaluated at $\overrightarrow{r_0}$. Accordingly, the tunneling current is proportional to the LDOS at the Fermi level, evaluated at the position of the tip. In terms of electron mass m_e, average work function ϕ, and sample-probe distance d, this expression can be further simplified:

$$I \sim V_G \exp\left(-\frac{\sqrt{8 m_e \phi}}{\hbar} D\right)$$

For typical values of work functions of roughly 4-5 eV,[30] a difference of 0.1 nm in the sample-probe distance will change the tunneling current by about an order of magnitude.

It is a notably popular misconception that STM images depict the purely geometric structure of the surface. While true on some surfaces, this interpretation is generally invalid. For conducting materials, STM image data coincides with the topography. However, for materials that are semiconducting or exhibit directional bonding, STM reflects a convolution of the surface topography and electronic structure. Similarly, the presence of adsorbates can alter the LDOS;[31] depending on the whether they enhance of deplete the LDOS at the Fermi level, they may be imaged as protrusions of depressions.

2.1.4 STM Movies

Using a combination of fast scanning rates and low temperature cooling, consecutive STM images may be collected in the same area of the sample and compiled into a movie. Using such a technique allows for the capture of dynamic processes – such as the diffusion of molecules – on the surface. An example of this is seen in Chapter 7, tracking the molecular motion of coronene molecules adsorbed on a Cu(111) step edge in order to characterize the one-dimensional intermolecular interaction. To counteract the distance drift between sample and probe, specialized pattern recognition software is implemented readjust the position of the probe and correct the movie data post-recording.

2.2 Scanning Tunneling Spectroscopy

An STM can also be used to acquire spectroscopic data in a manner referred to as scanning tunneling spectroscopy (STS).[21] If the DOS of the probe tip is kept constant, then the LDOS of a local area may be obtained by plotting the conductance I/V as a function of the varying voltage V. To understand this approach, we use the Wentzel-Kramers-Brillouin (WKB) approximation scheme suggested by Selloni *et. al.*:[32]

$$I \sim \int_{-\infty}^{\infty} \rho_S(r,E)\rho_p(r,E-eV_G)T(E,eV,r)dE$$

$\rho_S(r,E)$ and $\rho_p(r,E)$ represent the DOS of the sample and tip, respectively, at the location r and energy E with respect to their individual Fermi levels. $eV < 0$ and $eV > 0$ represent a negative and positive sample bias, respectively. The tunneling probability of electron must be a smooth, monotonically increasing function of V and can be expressed as:

$$T(E,eV) = \exp(-\frac{2z\sqrt{2m_e}}{\hbar}\sqrt{\frac{\phi_s+\phi_t}{2}+\frac{eV}{2}-E}\ )$$

Thus, the bias dependence of $T(E, eV_G, r)$ contributes smoothly varying background upon which the spectroscopic information of interest is superimposed. Differentiating the WKB approximation results in:

$$\frac{dI}{dV} \sim \rho_s(r,E)\rho_p(r,0)T(eV,eV,r) + \int_0^{eV} \rho_s(r,E)\rho_p(r,E-eV_G)\frac{dT(E,eV,r)}{dV}dE$$

Thus, dI/dV as a function of V can be attributed to the structure of in the DOS. Even so, the resulting information will always be a convolution of the electronic structures of the sample and the probe. It is important to characterize the influence of the probe's electronic structure and, if possible, obtain a tip with a featureless electronic structure. The state of the probe can be obtained by performing spectroscopy on a known surface, most commonly highly oriented pyrolytic graphite (HOPG).

When V becomes an appreciable fraction of the sample and probe work functions, complications often arise due to the strong dependence of $T(E, eV, r)$ on V. For metals and semiconductors, the energy range of interest often extends over several electron volts on either side of the Fermi level. Unfortunately, the V-dependence of $T(E, eV, r)$ may distort features in the STS. However, the division of dI/dV by I/V normalizes the spectrum, effectively cancelling out the exponential voltage dependence of $T(E, eV, r)$, and reflects the electronic density of states reasonably well.

2.3 Instrumentation

The work presented here uses data collected from an ultra-high vacuum (UHV) Omicron Nanotechnology Variable Temperature Scanning Probe Microscope (VT SPM) system. The following summary and schematic are based on the description provided in the system manual. Main components include:

- Piezo scanner – Made of piezoelectric material, this piece changes its length in response to an applied voltage and provides a fine adjustment of the STM probe position.
- SPM Pre Amplifier – This component amplifies the tunneling signal and converts it into voltage for image processing. The measured current is also used as feedback information by comparing to the desired current value and repositioning the tip.
- Z Regulator – This piece controls the sample-probe distance, minimizes the signal error based on input from the Pre Amplifier, and maintains the constant tunneling current.
- XY Scan Generator – This generator controls the raster scan of the probe in the plane of the sample. Scan speed, sampling, and size can be set by the user.
- XYZ Signal Image Processor – This component converts the raw data from the Scan Generator and Z Regulator into image information.

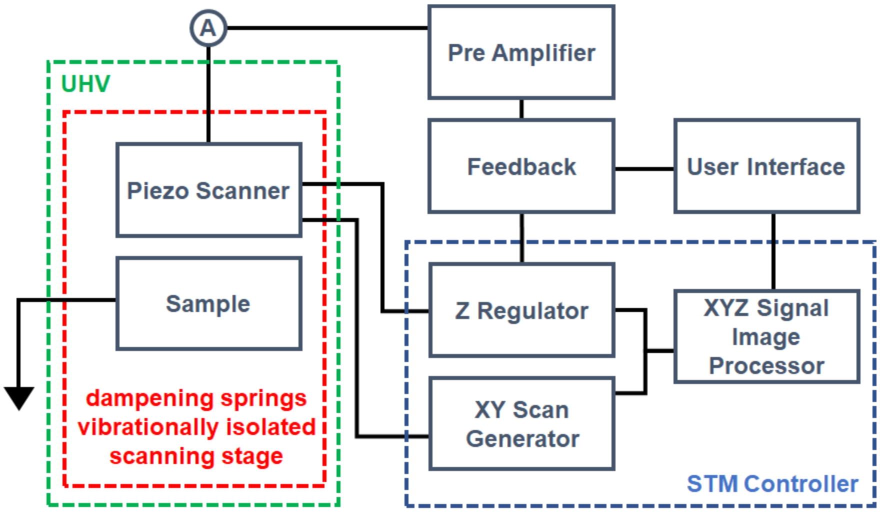

Figure 5: Diagram of the Omicron Nanotechnology VT SPM setup.

In addition, noise dampening is critical to the acquisition of high resolution images. To this effect, four soft springs suspend the scanning stage, which is also surrounded by a series of copper plates and magnets, which provide non-periodic eddy current dampening. The entire chamber rests on rubber padding and is located in a vibrationally isolated room. Base pressure for the system is approximately 8×10^{-11} Torr and experiments were performed at room temperature unless otherwise stated. STM probes were commercially prepared etched tungsten tips from Veeco (8mm, Model TT), mounted in Omicron STM tip holders, and outgassed at 120 °C for at least 2 hours before use.

Throughout this dissertation, the voltage bias between the sample and the probe will be referred to as V_G and the tunneling current will be referred to as I_t. Both parameters are set by the user and rely on software, STM controller, and feedback mechanism to implement while scanning. The STM itself is operated in constant current mode, allowing the tip to scan along the surface at a specified current. The STM's feedback mechanism adjusts the positioning of the probe normal to the sample surface as necessary to maintain this current, and this motion provides topographic information on the surface. Another mode of operation is constant z mode, where the probe is disengaged from any feedback loop, scans the surface at a set distance, and detects the changing tunneling current. However, this mode is not used here.

2.4 Other Surface Science Techniques

The experimental methods performed in this work consist primarily of surface science techniques and analysis. First and foremost, scanning tunneling microscopy (STM) is implemented to acquire high resolution, atomic-scale information on aromatic carbon materials of interest. As such, the primary focus of this chapter is to provide a background description of STM. In addition, other surface science techniques also play a fundamental role in the presented thesis work and will be described briefly as well:

- Scanning Electron Microscopy (SEM) – This type microscopy produces images of a sample by scanning the surface with a focused beam of electrons, which interact with atoms on the surface of a sample and produce various signals that contain information about the sample's surface topography and composition. Many systems are also equipped with energy-dispersive X-ray spectroscopy (EDS) systems that can obtain information on the chemical composition of the sample.[33–35]
- X-ray photoelectron spectroscopy (XPS) - Also referred to as electron spectroscopy for chemical analysis (ESCA), this is a widely used technique which uses X-rays to excite electrons in specific bound states. The specific energy of an elemental core level transition occurs at a specific binding energy which uniquely identifies and sometimes quantifies the element. Additionally, photo-ejected electrons from core levels have slight shifts depending on the outer valence configuration of the material examined, providing information on chemical bonding.[36,37]
- Raman spectroscopy – This spectroscopic technique observes vibrational, rotational, and other low-frequency modes in a system, which provides structural fingerprint by which molecules can be identified. Typically, a sample is illuminated with monochromated light, which induces inelastic (Raman) scattering. The laser light interacts with molecular vibrations, phonons or other excitations in the system, resulting in the energy of the laser photons being shifted up or down. The shift in energy gives information about the vibrational modes in the system.[38–40]
- Brunauer-Emmett-Teller (BET) Surface Area Assessment – Although invented in 1938 and despite making a few broad assumptions, BET theory one of the most frequently used models for gas adsorption mechanics.[41] To perform BET surface

area measurements, a sample is placed a vacuum system, a gas (often N_2) is leaked in, the amount of adsorbed gas is measured as a function of gas pressure, and this information is used to calculate the total accessible surface area. The use of the BET method for interpreting N_2 adsorption isotherms has become a standard protocol for assessing the surface area of highly porous media.[42]

CHAPTER 3: Computational Methods

3.1 Density Functional Theory

Using a first principles (*ab initio*, or "from the beginning") approach, the computational methods performed in this work are used to complement the experimental work described in the previous chapter. Because STM only interrogates the electronic structure of the surface, no direct conclusions can be drawn with regards to the chemical identity of the surface structures. Moreover, because STM reflects a convolution of the topographical and electronic structure of a surface, it is often difficult to correlate observed features with atomic structure. One of the most popular theoretical techniques, density functional theory calculations (DFT) mitigates this issue and often complements STM work. In 1998, Walter Kohn and John Pople were awarded the Nobel Prize in Chemistry in recognition of the many contributions DFT made towards the understanding of electronic properties of materials.[43] Popular amongst chemists, physicists, and materials scientists, DFT has the power to elucidate material characteristics such as energetics, geometric features, and electronic structure. Using the calculated electronic structure, one can extract the LDOS at the Fermi level of the system of interest, plot projected contour plots, and simulate constant current STM images.

In condensed matter physics, an *ab initio* approach starts with what is known about a system – in this case, atoms, their charges, masses, and the quantum mechanical interactions between them. The behavior of electrons determines the properties of most materials; unfortunately, in practice, solving the Schrödinger equation for each electron in a system is a time-consuming task that balloons when increasing complexity of the system. For example, solving the Schrödinger equation for hydrogen is often performed analytically as an early exercise in quantum mechanics coursework. However, solving for helium requires a computational approach.[44] Thus, it is critical to employ methods that efficiently, yet accurately describe the many-body problem of electrons in complex condensed matter systems.

3.2 Basic Equations of DFT

In order to describe any system of interacting atoms and electrons, one must refer to the time-independent Schrödinger equation:

$$\hat{H}\Psi(r_1, r_2, \dots . r_N) = E\Psi(r_1, r_2, \dots . r_N)$$

$\hat{H}$ represents the Hamiltonian operator, E is the energy of the system, and $\Psi(r_1, r_2, \dots . r_N)$ is the many-body wave function containing all information regarding the physical state of the system composed of N electrons. As the number of particles considered increases, the complexity of solving the Schrödinger equation increases rapidly. However, some of this complexity may be reduced by applying the Born-Oppenheimer approximation, which states that the motion of atoms relative to that of electrons is so slow that atoms can be considered stationary. This inhomogenous electron gas model is the principle theoretical representation of all condensed matter and molecular systems: electrons act as a set of interacting point charges moving through the potential field of a set of static atomic nuclei.

Further progress in solving Schrödinger's equation can be made by applying two theorems by Hohenberg and Kohn:[45]

- Theorem 1: The external potential of $v_{ext}(\boldsymbol{r})$ is a unique functional of the electron density $n(\boldsymbol{r})$.

- Theorem 2: The ground state energy can be obtained variationally; the electron density $n(\boldsymbol{r})$ that minimizes the total energy is the exact ground state density, where $E[n] = \int v(\boldsymbol{r})n(\boldsymbol{r})d\boldsymbol{r} + F[n(\boldsymbol{r})]$.

These theorems serve as the foundation for DFT. The first suggests that the Hamiltonian and, consequently, the total ground state energy can be expressed as a function of the electron density:

$$E[n] = T[n] + V_{ee}[n] + V_{ext}[n] = F[n] + V_{ext}[n]$$

$T[n]$ is the kinetic energy, $V_{ee}[n]$ is the electron-electron interaction energy, and $V_{ext}[n]$ is the energy associated with the external potential $v_{ext}(\boldsymbol{r})$. The second theory states that if $F[n]$ is known, then one can use minimization to solve for the exact ground state energy and electron density. The Kohn-Sham approach references a non-interacting system with the same energy as the interacting system, as described by:[46]

$$E[n] = G[n] + \frac{1}{2}\iint \frac{n(\boldsymbol{r})n(\boldsymbol{r}')}{|\boldsymbol{r}-\boldsymbol{r}'|}\, d\boldsymbol{r}d\boldsymbol{r}' + \int n(\boldsymbol{r})v_{ext}(\boldsymbol{r})\, d\boldsymbol{r}$$

The functional $G[n]$ does not depend on $v_{ext}(\boldsymbol{r})$ as $F[n]$ does. $G[n]$ is composed of two terms: the kinetic contribution from the non-interacting electron gas $T_s[n]$ and the exchange-correlation energy $E_{xc}[n]$. By construction, E_{xc} represents the difference between the exact ground state energy and the sum of the $T_s[n]$ and the $E[n] - G[n]$. By applying the variational principle, Kohn and Sham derived a set of single-electron Schrödinger equations, where the set of single-electron wave functions must correspond to the electron density, and produced the Kohn-Sham equations:

$$\left[-\frac{1}{2}\nabla^2 + v_{eff}(\boldsymbol{r})\right]\psi_i(\boldsymbol{r}) = \epsilon_i\psi_i$$

$$\sum_{i=1}^{N} |\psi(\mathbf{r})|^2 = n(\boldsymbol{r})$$

The effective potential $v_{eff}(\boldsymbol{r})$ is the sum of the total electrostatic potential and the derivative of the exchange-correlation energy:

$$v_{eff}(\boldsymbol{r}) = v_{ext}(\boldsymbol{r}) + \int \frac{n(\boldsymbol{r})n(\boldsymbol{r}')}{|\boldsymbol{r} - \boldsymbol{r}'|} d\boldsymbol{r}' + \frac{\partial \mathrm{E_{xc}}[\mathrm{n}]}{\partial \mathrm{n}(\mathbf{r})}$$

In DFT calculations, the Kohn-Sham equations are solved self-consistently by first choosing a trial $n(\boldsymbol{r})$, evaluating $v_{eff}(\boldsymbol{r})$ and a set $\psi_i(\boldsymbol{r})$, and then solving for a new $n(\boldsymbol{r})$. This process is repeated iteratively until convergence is reached and the total energy is then calculated as:

$$E = \sum_{i=1}^{N} \epsilon_i - \frac{1}{2} \iint \frac{n(\boldsymbol{r})n(\boldsymbol{r}')}{|\boldsymbol{r} - \boldsymbol{r}'|} d\boldsymbol{r} d\boldsymbol{r}' - E_{xc}[n] - \int \frac{\partial \mathrm{E_{xc}}[\mathrm{n}]}{\partial \mathrm{n}(\mathbf{r})} \mathrm{n}(\mathbf{r}) d\boldsymbol{r}$$

Although this method is exact, in real practice, the exchange-correlation energy must be approximated because its true functional form is unknown. The exchange-correlation energy results from the Pauli Exclusion principle, specifically arising from the fact that electrons with the same spin are separated by a repulsive exchange force. Kohn and Sham used the local density approximation (LDA) to treat E_{xc} as dependent on a slowly varying electron density:[46]

$$E_{xc}[n] = \int n(\boldsymbol{r}) \epsilon_{xc}(n(\boldsymbol{r})) d\boldsymbol{r}$$

Although this assumption is not true for surfaces whose electron density exponentially decreases into vacuum (following the decay of the wave functions), it has produced many results that quantitatively agree with experimental values for material physical properties, molecules and adsorbed species.[47] Unfortunately, it is weak approximation in some applications, most notably in the estimation of binding energies (overestimating on the order of 1-2 eV).[48,49]

The generalized gradient approximation (GGA) is considered more robust, and it treats E_{xc} as a function of both the electron density and the gradient of this density:

$$E_{xc}[n] = \int n(\boldsymbol{r})\epsilon_{xc}\big(n(\boldsymbol{r}), \nabla n(\boldsymbol{r})\big)d\boldsymbol{r}$$

GGA has its own strengths and weaknesses. For example, it produces erroneous results when the electron density varies too rapidly.

The calculations presented here were carried out using the gradient-corrected Perdew-Burke-Ernzhof (GGA-PBE) functional and, following the general standard, do not account for van der Waals interactions.[50,51] It is important to note that the self-consistent DFT energy represents the ground state energy at zero pressure and temperature.

3.3 Vienna ab initio Simulation Package

Additional progress was made by further developing approximations to make calculations more computationally feasibly while maintaining accuracy:

- Basis Set – define set of functions that can be linearly combined to constitute electron wavefunctions. Plane wave basis sets with periodic boundary conditions were adopted in favor over localized basis sets in order to better represent electron orbitals.[48]
- Pseudo-potentials – generally represent an effective interaction and include Coloumb, exchange-correlation, and other ionic contributions.[52] Psuedopotentials were derived to simplify the potential felt by valence electrons, accounting only for the active valence electrons while representing core electrons and atomic nuclei as

rigid ion cores (Born-Oppenheimer approximation). In 1990, David Vanderbilt developed ultra soft pseudo-potentials (US PP) that obtained smoother pseudo-wave functions using much fewer plane waves. US PPs produced accurate calculations comparable to the previously used, yet computationally demanding norm-conserving potentials.[53,54]

Developments in DFT, GGA, plane wave basis sets, and US PP led to the development of the Vienna *ab initio* Simulation Package (VASP), a commercially available software package written in FORTRAN by Georg Kresse and Jürgen Fürthmuller,[48] and based on software developed by Mike Payne that also contributed to the development of a similar package, CASTEP.[44] VASP performs theoretical calculations in the framework of DFT and GGA using the Perdew and Wang exchange-correlation (PW91) functional and the projector augmented wave (PAW) method or US Vanderbilt pseudo-potentials.[53–55]

VASP applies a self-consistent, iterative scheme that cycles through charge density optimization and wave function optimization. Beginning with a trial set of charge density and wave-vectors, VASP will perform sub-space rotation, minimization, orthonormalization using a Gram-Schmidt method, and an update of the partial occupancies and charge density, looping until convergence of the estimated free energy is achieved.

The computational work of this thesis implemented VASP 5.4.4, installed on the Stampede 2 cluster of the National Science Foundation's (NSF) Extreme Science and Engineering Discovery Environment (XSEDE). Running a typical VASP calculation requires four files:

- POSCAR – specifies the initial atomic coordinates and unit cell size.
- POTCAR – describes the pseudo-potential for each element.

- INCAR – defines calculation parameters and desired algorithms.
- KPOINTS – specifies sampling of the inverse space.

The typical output files of interest are CONTCAR and OUTCAR, which contain information of the final relaxed geometry of the system and information regarding convergence, respectively. In addition, the following output files are useful:

- WAVECAR – provides information on the wavefunctions.
- DOSCAR – describes the DOS information for each atom.
- CHGCAR – provides information on the charge density.

3.4 Preliminary Studies

Preliminary exercises were performed on simple systems well studied in the literature in order to ensure a complete understanding of VASP, its input parameters (INCAR), and the system of interest. The reproducibility of well-known results confirmed the reliability of new findings.

3.4.1 Pristine and Single Vacancy Graphene

Theoretical efforts presented in this thesis are focused on catalytically enhancing the otherwise chemically inert graphene surfaces through impregnation with platinum nanoparticles. However, first, it is important to confirm the reliability of DFT calculations on graphene. To start, common graphene-based systems were optimized and their DOS plots were generated to reproduce results from the literature for pristine, nitrogen-doped, and boron-doped graphene.[56]

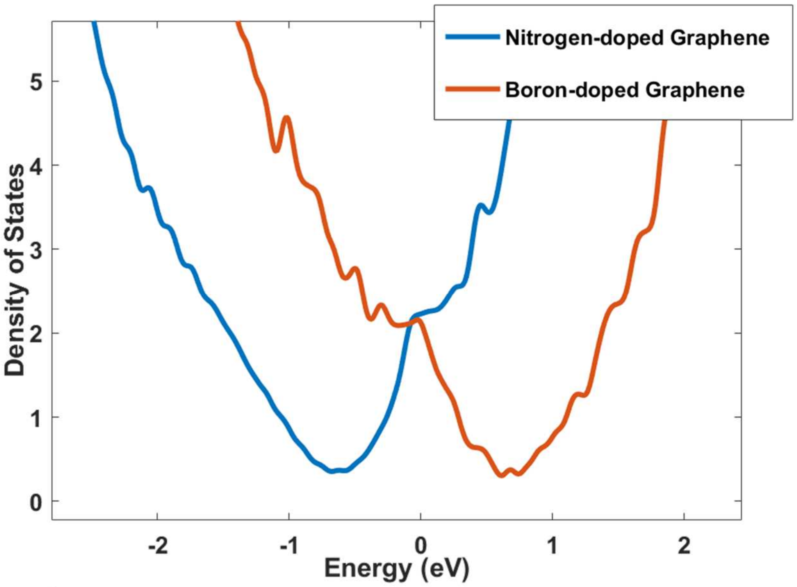

Figure 6: As shown in the density of state plot above, graphene's unique, characteristic Dirac cone then shifts lower or higher. (Notably, ripple features indicate that increased k-points should be used, but for demonstrative purposes, the computation exhibits the overall linear behavior and shifts expected.)

In addition, preliminary tests were performed on a single platinum atom anchored on a single vacancy graphene. Calculations settings were tested to see what constraints and approximations were necessary to obtain good accuracy. As shown in the Table, at some point, increasing either k-points or energy cutoffs results in an accuracy improvement of less than 0.02 eV (as seen in the table below), a value represents the resolution limits of DFT.

k	eV	ENCUT	eV	EDIFF	eV
2x2x1	-655.20	450	-654.67	1.00E-05	-654.91
4x4x1	-654.53	500	-654.53	1.00E-06	-654.53
9x9x1	-654.53	550	-654.54	1.00E-07	-654.53

Table 1: VASP results for platinum on single vacancy graphene, varying parameters for increased accuracy during system optimization.

Both LDA and PBE were compared. LDA is known to produce results more comparable to experimental findings for graphene;[57,58] however, PBE is more widely used in the literature, useful for better estimating binding energies, and accurate at describing metal nanoclusters.[59] When comparing against findings in the literature for predictions of Pt-C distance and Pt binding energy on single vacancy graphene, better results were achieved with PBE.

Author	Pseudopotential	Pt-C distance	Binding Energy
Kong	GGA	1.93	-7.7
Krasheninnikov	PBE	1.95	-7.5
Tang	PBE	--	7.234
Wang	PBE	1.94	-7.2
Wang	LDA	1.91	-8.98

Table 2: Comparison between preliminary results (Wang) with those from previous studies (Kong, Krashninnikov, and Tang).

Again, DOS plots were generated to reproduce those from the literature.

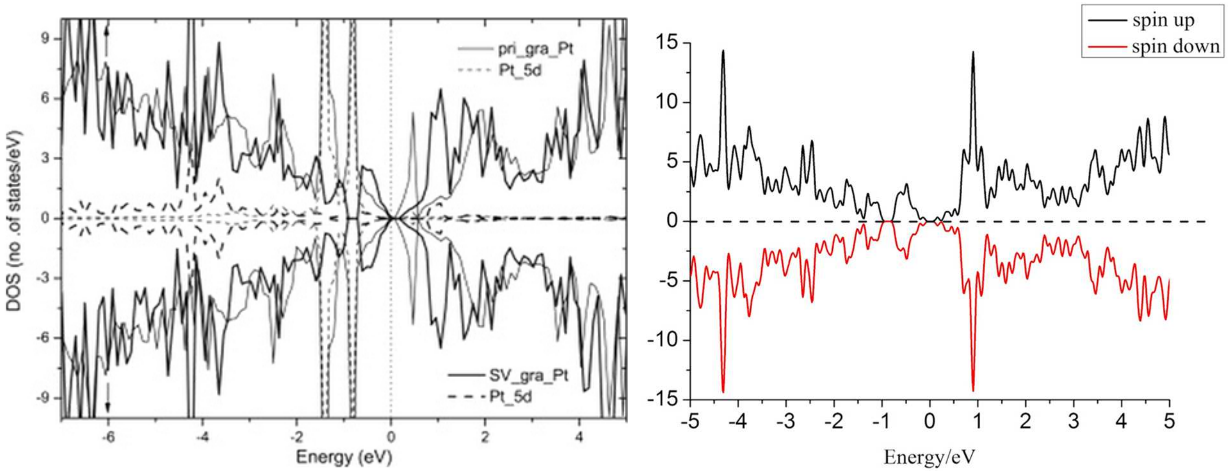

Figure 7: Comparison of density of states for platinum adsorbed on a single vacancy from Tang et. al. (left, thick line) and our preliminary results (right).

Generally, simulations were constructed using a 6 × 6 graphene super cell and optimized with a 3 × 3 × 1 k-point mesh (over reciprocal space), a 500 eV energy cutoff

(ENCUT), and an allowed error of 1×10^{-7} in total energy (EDIFF). These parameters are similar to those chosen for similar DFT studies.[60–64] Electronic information, such as density of states and charge density plots, use a 9x9x1 k-point mesh to provide enough resolution to capture important features.

CHAPTER 4: Revealing the Molecular Structure of Soot Precursors

4.1 Understanding Soot Formation

Reducing the amount of soot in the environment is desirable for many reasons. For instance, soot particles are believed to adversely affect human health when inhaled.[65] Soot contamination of snow and ice contributes to an average global temperature increase, while the net effect of soot in the atmosphere is potentially large but less well established. Thus, there has been a large number of studies over the past fifty years into the mechanisms of soot formation.[66–68] Of the many processes during soot evolution, starting with chemical reactions between small molecules and ending with the formation of sometimes micrometer-sized soot aggregates, it is the crucial step of particle inception that is perhaps the least understood. One intriguing hypothesis suggests that soot inception is triggered during combustion when planar polycyclic aromatic hydrocarbons (PAH) molecules, each containing 20-30 carbon atoms, begin to condense into small clusters.[69] This initial aggregation process is not well understood, yet it is crucial to predicting when soot forms. The fundamental impediment to progress is familiar to nanoscience: the arrangement of a few molecules assembled into a small particle can be very different from that in an easier-to-image macroscopic particle.[70] Furthermore, predicting the low-energy configurations of molecule clusters can be exceedingly difficult, especially if they are dominated by long-ranged van der Waals or electrostatic interactions.[71] A promising route to progress is to image the PAH clusters and to compare their structure with theoretical predictions.

Although transmission electron microscopy has been used to characterize the final structure of mature soot in great detail,[72] it has not been able to resolve the structures of the 2-5 nm wide clusters involved in soot inception. Atomic force microscopy[73–76] has confirmed the existence of small particles in flames and inspired conjectures of the particles' internal structure,[77,78] but has not yet imaged them with molecular resolution.

The crucial question about the clusters' structure is how ordered the molecules are arranged in them. In particular, is there a preferred orientation of the molecules at their surface? This knowledge is critical in understanding how additional molecules are incorporated into the clusters, and thus determines how and when the clusters will evolve into mature soot. In mature soot, the "primary" particles have an onion-like structure in which graphitic layers are oriented nearly parallel to the particle surface. It is unknown if this is also true for incipient soot particles. Recent theories of nanoscale coronene clusters[79] have proposed that the ground state of clusters containing tens of PAH molecules can be very disordered and bear little resemblance to bulk crystalline structures. Because of the large number of degrees of freedom, finding the lowest energy configurations of a few PAH molecules is a daunting problem, even when using simplified intermolecular potentials.[80] Further, the nature of the configurations has been found to depend sensitively on the details of the intermolecular potential.[81] This complexity drives the need for experimental data on the molecular structure of these clusters.

Our approach to determining the clusters' structure is to deposit PAH molecules on a surface where atomic resolution scanning tunneling microscopy can be used to examine how the molecules move and interact as they form clusters. This low temperature surface environment is of course considerably different than the 1000-2000 K gas of dilute PAH molecules in a flame; even so, we will show that this system sheds insight into the ground state structures involved in soot inception.

The adsorption of PAHs has been extensively studied on many surfaces.[82] Most of this past work has focused on the interaction of the PAH molecules with the substrate. For example, determining the strength of their interaction with metal surfaces is important in understanding catalytic reactions of these molecules. In this work, we focus instead on the interaction between the PAH molecules themselves, and on how this affects their aggregation. We chose to study the PAH molecule coronene, $C_{24}H_{12}$, as its size is characteristic of the molecular building blocks of incipient soot.[68] We conducted our experiments on Pt(111) and Cu(111) surfaces. Past work has shown that hydrocarbons interact more strongly with Pt than with Cu,[83] so these two substrates were selected to facilitate gauging the impact of substrate interaction on the cluster geometry.

We find that when deposited on Pt(111) at room temperature, coronene initially decomposes to form a "soup" of various PAH molecules similar to what might be encountered in a flame. Molecules deposited on top of this layer form small clusters containing several coronene molecules. We use density functional theory to explain the structure and stability of these extremely small clusters. On heating to moderate temperatures, the clusters gradually increase in size, eventually forming complex disordered clusters of 20-100 molecules with a shape similar to those that have been proposed for incipient soot, as discussed in further detail below. Remarkably, very few coronene molecules at the surface of these clusters are oriented parallel to the surface. In contrast, on Cu(111), coronene does not decompose, and instead forms an extremely well ordered monolayer. Diffusion of coronene on top of this ordered layer is so fast that it leads to the immediate formation of macroscopic bulk coronene at room temperature. The structure of the initial clusters could not be observed.

Our experimental approach is to create 3D clusters of PAH molecules by deposition. 3D clusters are not expected to form at submonolayer coverages because hydrocarbons generally first form a 2D wetting layer on metal surfaces. However, since this monolayer is likely to be the substrate for subsequent cluster formation, it is important to characterize it in detail.

4.2 The Molecular Wetting Layer of Coronene on Pt(111)

As described in greater detail in the Methods sections, repeated deposition of coronene via thermal evaporation achieved increasing levels of sub monolayer coverage on the Pt(111) surface, and STM imaging verified the adhesion of the molecule to the surface. Figure 1a shows sub-monolayer coverage of coronene, in which a hexagonal 2D molecular structure is observed with three ripple-like stripes across it. These stripes are attributed to rows of benzene rings aligned with the close-packed Pt(111) directions ([-1 1 0] and equivalent), and these features are consistent with other STM investigations of coronene.[84–87]

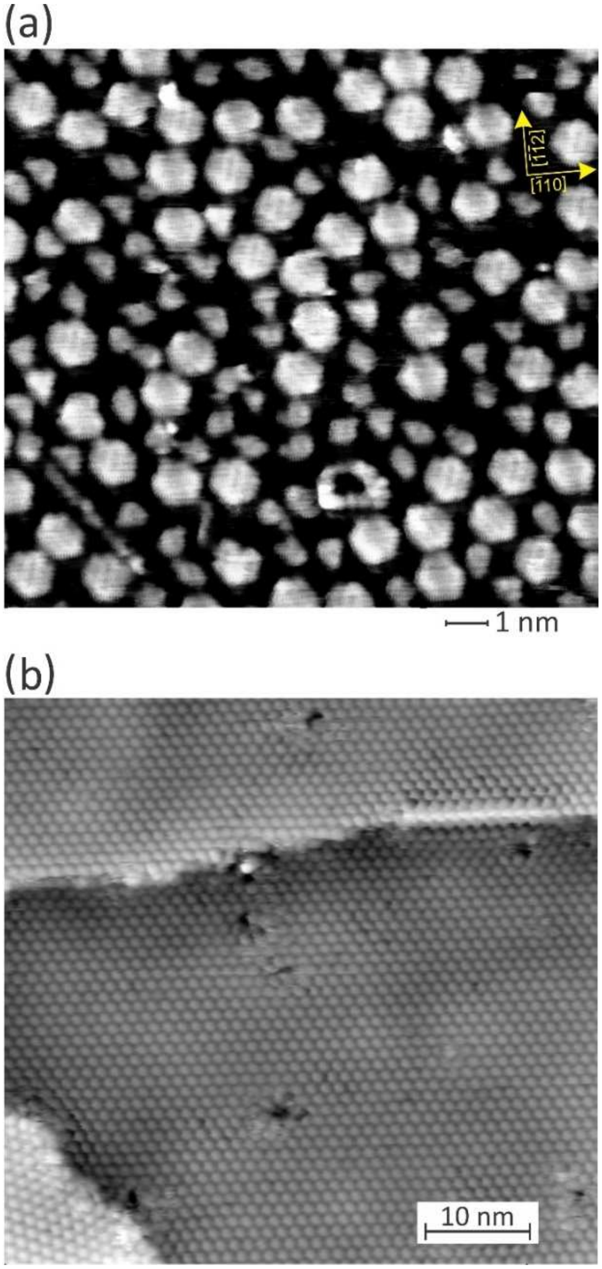

Figure 8: (a) STM image of the arrangement of coronene molecules and its fragments on a Pt(111) surface. Sample bias: -0.1 V; Tunnel current: 400 pA. (b) STM image of a saturated molecular layer of coronene molecules on a Cu(111) surface. Sample bias: 1 V; Tunnel current: 100 pA.

Furthermore, STM revealed that some of the coronene molecules decomposed into fragments, as shown in Figure 8. Comparison with DFT calculations allowed us to identify these fragments as predominantly triphenylene, pyrene, as well as benzene chains of varying length, similar to naphthalene, anthracene, and tetracene. The apparent heights of these molecules are relatively low (0.15 nm), which show strong binding to the substrate, a result that is consistent with DFT calculations. Figure 9 shows DFT image simulations of the PAH molecules on Pt(111). Notice that the simulation of the coronene molecule centered on a Pt bridge site reproduces the two-fold (striped) symmetry of the experimental images. Matching the orientation and symmetry of the triphenylene molecule requires centering it on a threefold hollow site. Occasionally, clusters around 0.5 nm in height and 2 nm in width, often resembling graphene patches, were observed scattered about the surface (not shown).

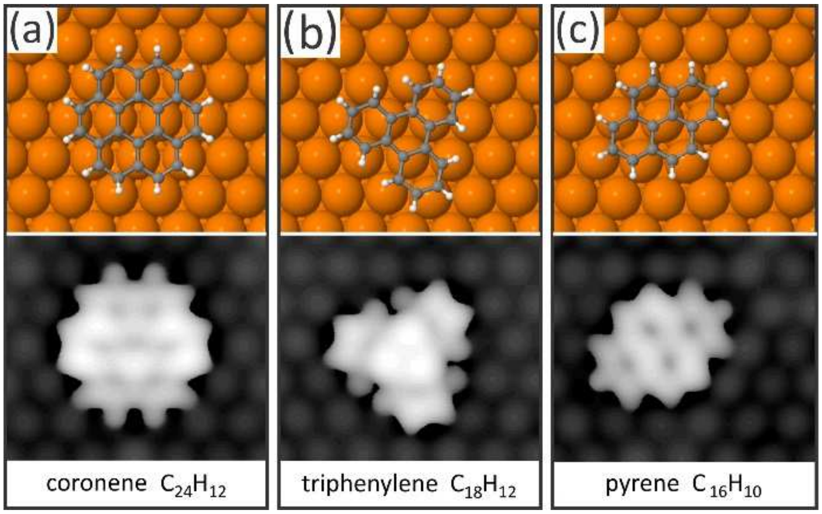

Figure 9: (top) Structure models of the PAH molecules observed in Figure 8 on Pt(111), along with the STM image simulations (bottom) generated with DFT by determining the contour of constant integrated electronic charge density between the fermi level and 0.1eV below.

As more coronene is deposited, the surface coverage increases and a higher fraction of coronene molecules remains intact. However, the initially produced fragment molecules appear to prevent the establishment of any long-range ordering on the surface. In instances where coronene molecules neighbor each other, as seen in Figure 8a, they typically exhibit a set spacing of ~1.1 nm from center to center of neighboring molecules, suggesting a repulsive intermolecular interaction. This distance is consistent with that measured for coronene on graphite and MoS_2 substrates.[88] Similar behavior has been previously observed for both coronene and similar PAH molecules adsorbed on bare metal surfaces such as Ag(100), Ag(111), and Cu(111).[89,90]

To examine how much the presence of the substrate affects the evolution of coronene clusters we deposited coronene under the same conditions onto Cu(111). As seen in Figure 8b, the coronene molecules self-assemble into a highly ordered two-dimensional arrangement without any evidence of fragment molecules, consistent with prior literature.[81] We measured the spacing between neighboring molecules to be (1.25±0.1) nm, which is only slightly larger than the spacing on Pt(111). Unfortunately, deposition on top of this layer at room temperature immediately created macroscopic coronene crystals that were visible optically. (Presumably coronene diffusion on top of the ordered coronene substrate is so rapid that small clusters were not formed or decayed too rapidly to be observed.) The subsequent discussion of cluster formation thus focuses on experiments performed on Pt(111).

4.3 Beyond the First Molecular Layer

It is difficult to deduce the exact coverage of the disordered and inhomogeneous wetting layer. In this paper, we consider the monolayer complete at the inception of a second molecular layer. The structure of the second and further additional layers, which lack direct contact with the substrate, should be dominated by PAH interactions. How do the molecules arrange themselves under these conditions?

Van der Waals interaction favors molecule stacks that maximize contact area. Typically, PAH molecules can lower the electrostatic repulsion without seriously affecting the van der Waals attraction by a shift or rotation that places the hydrogens of one molecule roughly over ring centers of the other,[91] forming "parallel-displaced stack" configurations. However, as explained by Obolensky *et al.*'s[92] electrostatic ring model, the round shape of the coronene molecule renders such shifts or in-plane rotations much less effective in decreasing the Coulomb repulsion. As a result, T-shaped "edge-to-plane" configurations, which minimize electrostatic repulsion at the cost of giving up some of the van der Waals attraction, could become energetically favorable.

Does such interplay between electrostatic and van der Waals forces affect the coronene multilayers we grow on Pt? Figure 10 shows the typical morphology of 1.1 ML of coronene. The bright features represent intact coronene molecules residing in the second layer. Apparently, coronene decomposition is deterred, likely due to the "screening protection" provided by the first layer. We propose that most of these bilayer configurations (which appear as protrusions in our STM images) are manifestations of the two structural motifs discussed by Obolensky,[92] the "parallel-displaced stack" and the T-shaped "edge-to-plane" configuration.

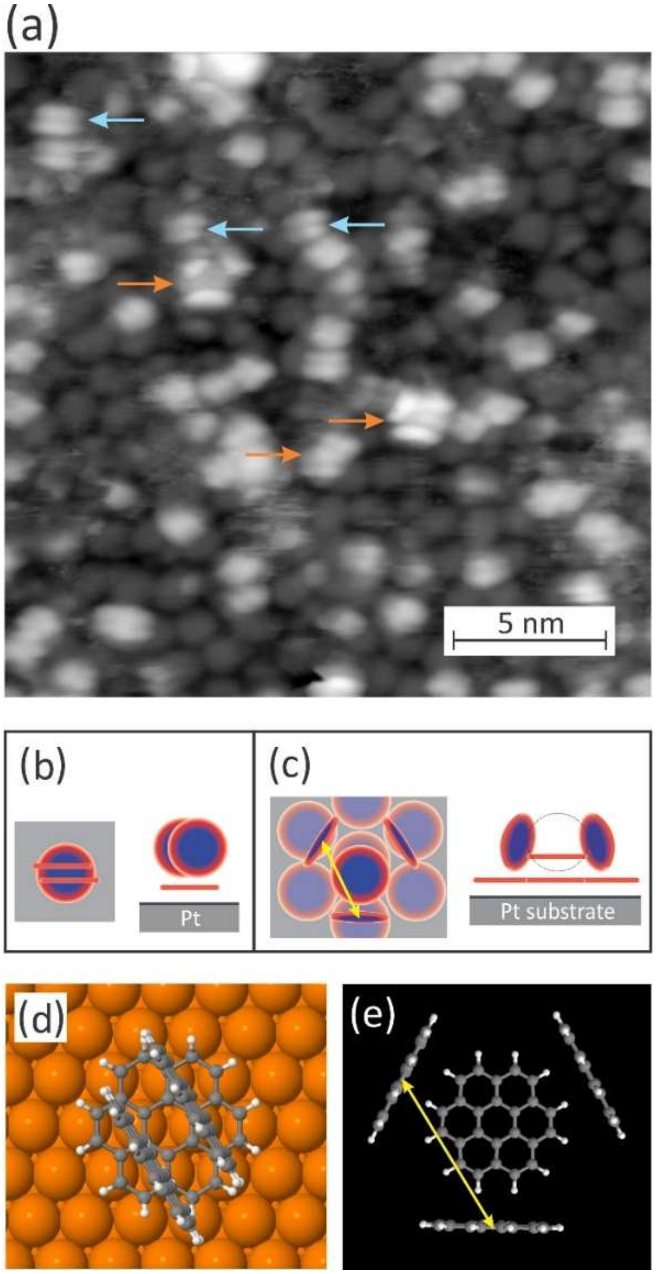

Figure 10: Second-layer configurations of coronene/Pt(111). (a) STM image of 1.1 molecular layers of coronene on Pt(111). Sample bias: -1 V; tunneling current: 200 pA. Light blue arrows mark examples of the "double" structure, orange arrows highlight examples of the "satellite" structure. (b) and (c) Schematics of the "doubles" and "satellites", in which each coronene molecule is represented by a disk. The color scheme, blue for the negatively charged interior and red for positively charged perimeter, has been adopted from Forker et al.21 (d) and (e) Top views of "double" and "satellite" structure, relaxed with DFT. In the "satellite" structure, the experimentally observed separation between upright coronene molecules (as denoted with a yellow arrow) is 1.33 +/- 0.15 nm, while our DFT calculation predicts 1.4 nm.

A schematic of the most common bilayer structure (marked by blue arrows in Figure 10a, referred to here as "doubles", is depicted in Figure 10b. Here, two coronene molecules, residing in the second layer, stand upright and are stacked slightly offset from each other in a parallel-displaced manner. (This second-layer dimer thus forms a parallel-displaced stack.) When such a dimer of upright molecules sits on a flat-lying first-layer molecule, the three molecules together form an “edge-to-plane” motif, with the second-layer dimer contributing the “edge” and a first-layer molecule the “plane”.

Another commonly observed structure is the “satellite structure”, marked by orange arrows in Figure 10a, and shown as a schematic in Figure 10c: A flat-lying second-layer molecule (the “center”) is surrounded at its perimeter by two to four nearly-upright second-layer molecules (the “satellites”). Here, the center molecule contributes the edge, and the upright “satellites” the “planes”. Presumably, the center molecule also participates in a parallel-displaced stack configuration with a first-layer molecule below. The upright satellites presumably also contribute the “edge” to “T” joints with first-layer molecules below. (The latter two assumptions, which cannot be verified because the buried first-layer molecules are inaccessible to STM, are not crucial for our arguments.)

To test our interpretation of the experimentally observed second-layer features, we relaxed “double” and “satellite” configurations in DFT, shown in Figures 10d and 10e. Both structures are found to be at least metastable, and DFT reproduces the stack spacing of 0.34 nm in the “double” and the measured average distance of 1.33 nm between the centers of the “satellites” (in the “satellite” configuration), corroborating our structure models depicted in Figures 10b and 10c.

Continued deposition revealed that the sticking probability of the coronene decreases with increasing coverage; finally, the coronene surface coverage saturated at approximately 1.3 molecular layers.

4.4 Emergence of Soot Precursors Upon Annealing

All of the surface configurations described above are likely to be governed by the limited mobility of PAHs at room temperature. At no time did we observe PAHs move on the Pt(111) surface. In order to make larger clusters further along the path to soot particle inception, we gradually enhanced surface mobility by slowly heating the saturated surface.

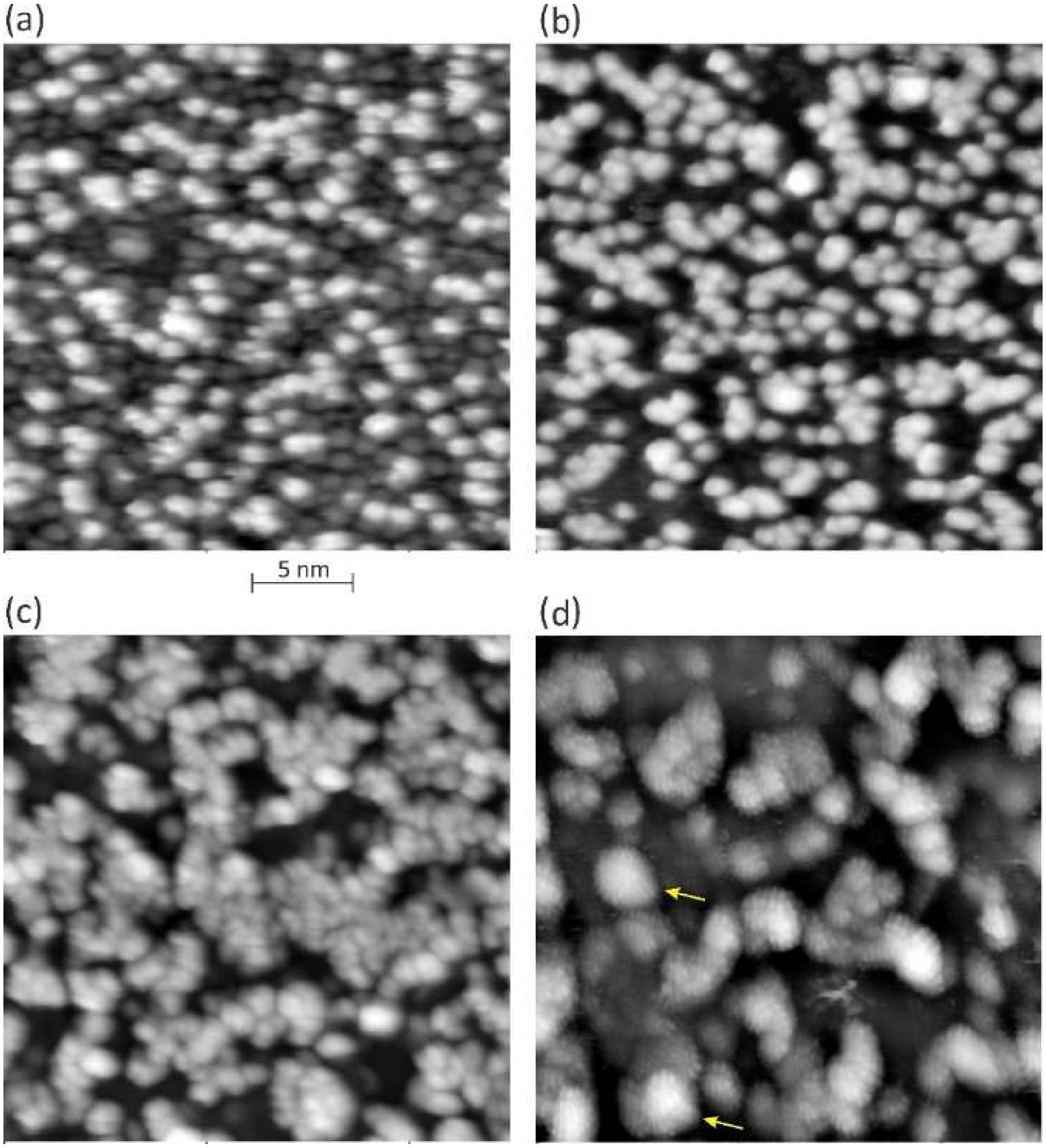

Figure 11: STM images of coronene/Pt(111) at: a) 70°C, b) 120°C, c) 360°C, and d) room temperature after heating to 540°C (V = -1 V, 100 pA, 20 x 20 nm). Yellow arrows point to molecularly-resolved clusters which are discussed in the text.

We heated from room temperature to 430˚C in 10 degree steps before a final 5 minute anneal at 540˚C. Slow heating and in situ observation (except for the final anneal) allowed STM to track the structural reformation. This process took place slowly, and there were no abrupt changes in the surface structures until the final anneal. The sequence of STM images of Figure 11, acquired after annealing to 70˚C, 120˚C, 360˚C, and 540˚C, captures the major steps of surface progression: At the lowest temperature of 70˚C, shown in Figure 11a, more coronene molecules had begun to flip up to form the “double” structure described previously. The first layer also partially dewets supplying the second layer with additional molecules. Satellite structures are more difficult to locate, confirming their relatively low thermodynamic favorability. At 120˚C (see Figure 11b), most “double” structures have gathered into short chains, which occasionally have side branches or are curled up into compact ~2 nm wide knots. Upon raising the temperature to 360˚C, the coronene chains have extended and no longer exhibit pairing. Rather, these chains have stacks of coronene similar to first-layer configurations found on Ge(001)[93] which have merged into a continuous network, depicted in Figure 11c. Neighboring chains often twist around each other, and more instances of larger, tightly packed bundles appear. At this point, all isolated “doubles” and “satellite” structures have vanished.

Finally, at around 540˚C, the coronene had bunched up into aggregated three-dimensional super-structures, shown in Figure 11d. These clusters exhibit a grape-like appearance and are typically 2 to 3 nm wide. Imaging three-dimensional features with STM is challenging because the surface morphology is convoluted with the shape of the tip, which often obscures important details of the measured surface structure or produces “ghost” artifacts. This difficulty is compounded by the poor electrical conductance of coronene causing the imaging STM tip to approach the surface more closely to maintain a constant tunneling current, which makes it challenging to avoid destructive tip-sample interactions.

Despite these obstacles, we were able to image some of the 3D clusters with sufficient resolution to make inferences regarding their internal structure. Two examples, marked by arrows in Figure 11d, are shown at higher magnification in Figure 12 (a,b). The surface of these coronene aggregates is corrugated—it consists of several sets of ~1 nm long ridges. The separation between these nearly parallel ridges was measured to range from 3.5 Å to 4 Å. Because of the relatively high concentration of coronene observed on the substrate surface before annealing, we believe that that these clusters are composed primarily of coronene molecules. The previously observed fragment molecules are possibly tightly bound to the active platinum surface and thus unable to participate in clustering. By assigning each of the observed nanoridges to an individual coronene molecule, we constructed approximate models for the internal structure of the coronene aggregates. In the model schematics depicted in Figure 12c and 12d, each coronene molecule is represented by a blue/pink disk 1 nm in diameter. While these model schematics include only the upper portions of the 3D clusters accessible to the probing STM tip, we assume similar arrangements of molecules to continue into the central and lower portions of the clusters.

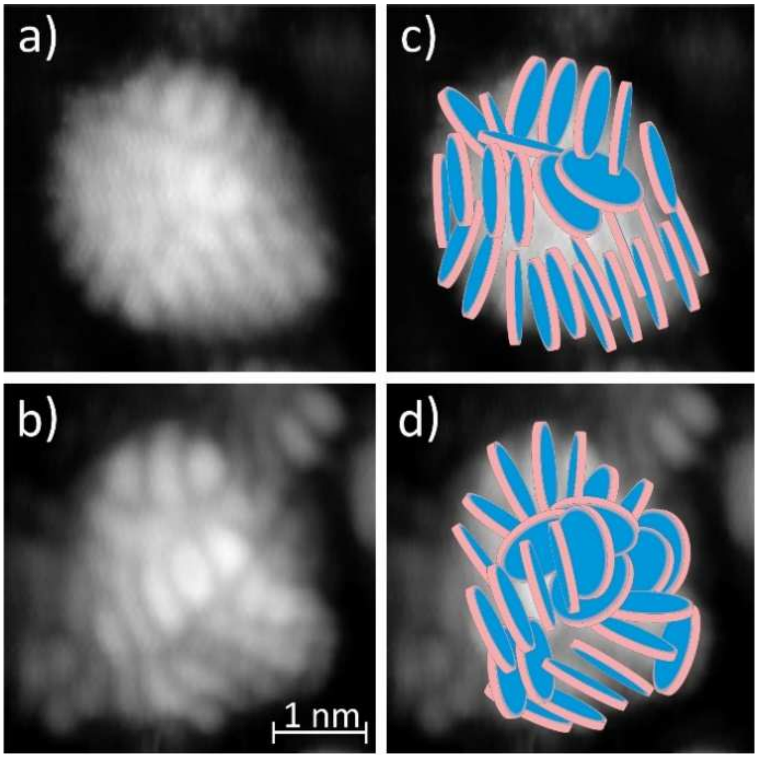

Figure 12: Internal structure of 3D coronene aggregates. a) and b) Detailed STM images of individual 3D coronene aggregates, extracted from the data shown in Figure 11d. c) and d) Estimated internal structure of these aggregates, deduced from the ripples seen in a) and b). In these schematics, each coronene molecule is represented by a blue/pink disk with a diameter of 1 nm.

Key features of the aggregates' structure are the following. The aggregates are composed of randomly oriented short stacks consisting of up to 5 molecules each. Within each stack, the molecules are nearly parallel, however their orientation can gradually change from molecule to molecule. Within a stack, molecules are slightly shifted laterally, *i.e.* within the plane of the molecule, with respect to their neighbors. These small variations in molecule shift and orientation, consistent with the measured separation between the nanoridges ranging from 3.5 Å to 4 Å, allow the molecule stacks to wrap around each other. Presumably, this flexibility and the variability in stack size facilitates the self-assembly of randomly oriented coronene stacks into 3D aggregates of the observed rather compact overall shape.

All the structural features described above match those of small coronene stacks[74] wrapping around each other as predicted by Totton *et al.*[80] and Pascazio *et al.*[81] for nascent soot particles. Experimental examination of the detailed structure of nascent soot generated in flames has not been possible to this date. In order to obtain microscopy results, the nascent soot particles must be deposited from flame on appropriate substrates. However, because these particles are liquid-like and weak in structure, they will flatten upon impact with the substrate, as AFM results by Barone *et. al.*,[73] Abid *et. al.*,[74] and Schenk *et. al.*[75,76] reveal. Hence, our experimental data represents the most detailed experimental information to date about the possible internal structure of incipient soot particles.

A notable feature of the coronene clusters observed on Pt is that only a very small fraction of the cluster-surface molecules is oriented parallel to the surface. This is dramatically different from mature soot, where the spherical primary particles have an "onion structure" with almost all benzene rings nearly parallel to the particle surface. This has important implications for the growth of these particles: When an additional coronene molecule collides with such an incipient soot particle, it will not be able to simply stack parallel to an existing coronene molecule. Whether the new molecule is bound strongly enough to irreversibly attach to the particle and grow it will depend on the energy of "T" configurations or require the incipient soot particle to rearrange to accommodate it.

4.5 Experimental Methods

All sample preparation was performed in ultra-high vacuum (UHV) conditions in the low 10^{-10} mbar range. The platinum substrate was prepared through continuous 5 minute cycles of 1500 eV neon sputtering and annealing at 900˚C. The copper substrate was prepared via similar means, annealing at 300˚C. Thereafter, the bare metal surfaces were kept at room temperature during deposition of coronene through thermal evaporation of the molecule at 120˚C using a boron nitride thermal effusion cell. Coronene (sublimed, 99 %) was purchased from Sigma Aldrich. For analysis, the sample was transferred to a variable temperature STM (Omicron), without the interruption of vacuum, and imaging was performed under 3×10^{-11} mbar conditions. Low energy electron diffraction and Auger spectroscopy measurements verified the cleanliness and quality of the sample surface. Heating experiments were first performed in the STM stage using the heating element of the sample holder. To anneal to higher temperatures, the sample was then transferred to the chamber manipulator.

DFT calculations were performed using the Vienna Ab-Initio Simulation Package.[94] All of the calculations were on a (6x6) substrate surface unit cell with three atomic layers of metal. Optimizations applied a $2 \times 2 \times 1$ k-point mesh, a 700 eV energy cutoff and structures were relaxed until forces where less than 0.1 eV/Å. The optimized van der Waals functional optB86b[51] was used. Dipole corrections were taken into account for both the local potentials and total energies. In addition, a vacuum length of at least 15 Å separated the slab from cell boundaries perpendicular to the surface.

4.6 Conclusion

In summary, we have used STM and DFT techniques to characterize the formation of molecular clusters of coronene on Pt(111) and Cu(111) surfaces. On Pt(111), we find that the substrate initially reacts strongly with the coronene molecules, as shown by the decomposition of coronene into fragment molecules. We propose that this interaction is inhibited once a monolayer coverage provides screening protection for subsequent molecular adsorption. At the bilayer, we observed parallel-displaced coronene pairs that assembled into chains, which first grew longer and then wrapped around themselves forming larger clusters as the surface temperature continued to increase. Upon annealing to 540°C, the coronene molecules transformed into large 3D clusters that bear strong resemblance to proposed incipient soot particles. A notable feature of these particles is that they have the opposite structure to large soot particles: rather than the coronene planes parallel to the surface, as in mature soot, they are largely perpendicular. This has important implications about how additional PAH molecules attach and get incorporated into the growing incipient soot particles. For example, the rate limiting mechanism for the initial stages of soot growth is likely to be a complex cooperative process as the PAH cluster evolves, and unlikely to be governed by a single simple barrier to PAH attachment. The configuration we observe is also likely to be important in soot chemistry – for example soot oxidation rates are believed to be highly sensitive to the surface configuration.[95] While our observations add credibility to the hypothesis that soot inception *can* occur via aggregation of planar PAHs into nanoclusters, additional experiments would be needed to test alternative mechanisms for the initiation of soot. One hypothesis is that radical sites at the perimeters of PAHs facilitate their growth into large non-planar molecules.[67] It would thus be instructive to perform similar studies with a variety of PAH and aliphatic molecules,[96] to assess how the shape and chemistry of the molecules affect their ability to aggregate into nanoclusters. Our success in obtaining molecular resolution of coronene clusters suggests that these experiments are feasible. Successive STM experiments might attempt to molecularly resolve the structure of flame generated clusters deposited on substrates.[76,77]

CHAPTER 5: Single Atom Pt Catalyst on Modified Graphene Supports

Inspired by visions of achieving the ultimate cost-effectiveness and efficiency in chemical reactions, this works provides a first principles study of single platinum atom catalyst. Density functional theory calculations explore the catalytic activity enhancement of a platinum atom through the use of a graphene support structure. This support structure is modified via defects and dopants to produce systems commonly observed during chemical vapor deposition graphene growth; specifically, pristine, single vacancy, and pyridinic N-doped graphene are compared. This work evaluates the stability of the single atom by characterizing the interaction of Pt atoms at neighboring stable sites and the tendency towards clustering. Finally, the electronic structures of Pt on single vacancy and pyridinic N-doped graphene are compared and used to provide insight into the catalytic oxidation of CO. Results suggest that pyridinic N-doped graphene is a promising candidate to support a single Pt atom as a catalyst for enhancing CO oxidation efficiency.

5.1 Towards Single Atom Catalysis

Supported noble-metal catalysts – such as platinum, gold, and palladium – are popular in industry due to their high activity and selectivity for a wide range of chemical reactions. Applications include chemical transformation, energy conversion, and environmental remediation.[97–103] However, no matter its size, a catalyst always interacts with reactants with its surface-most atoms; consequently, any atoms that inaccessible in the metal bulk are largely wasted. Inspired by visions of ultimate cost-effectiveness and efficiency in chemical reactions, numerous studies have explored the promise of reducing the standard catalyst – platinum – down to a single atom.[104–109] In this pursuit, graphene is a promising support structure due to its naturally high surface area and chemical inertness. However, the support must interact with the catalyst in a way that stabilizes it and promotes resistance to poisoning. The strong interaction between vacancies and dopants with metallic impurities addresses these issues as well as significantly influences the electronic and chemical properties of graphene, transforming the inert graphene into a very active catalyst. For example, gold, copper, and iron-embedded graphene systems have been predicted to catalyze the CO oxidation reaction.[110–112] Building upon these successes, the work presented here investigates the ability to stabilize clusters of few atom Pt down to a single atom and compare relative catalytic activity through the use of dopants and defects in the graphene lattice.

Pt is chosen because it is the most commonly used catalyst. Prior theoretical and experiments efforts demonstrating the controlled deposition, tunability, and catalytic activity of Pt via modification of graphene-based support structures.[113–117] However, it is well known that Pt and other metals tend to form clusters on pristine graphene surfaces,[118,119] and so the methods address this issue by evaluating the tendency towards clustering when Pt atoms neighbor each other at stable sites. First, Pt on graphene is used as a control system assess the viability of this model. Second, this model is used to assess the stability of Pt on single vacancy and pyridinic N-doped graphene (SVG and PNG, respectfully), both of which are often produced through common graphene synthesis procedures such as chemical vapor deposition. Finally, the electronic structure and catalytic ability of these systems are evaluated; specifically, the catalytic oxidation of CO is used as a test case. Results suggest that Pt_1/PNG is a promising candidate for enhancing CO oxidation efficiency.

5.2 Computational Methods

The Vienna ab initio Simulation Package (VASP) implementation of density functional theory was utilized to perform all calculations presented here.[48,120] Projector augmented wave (PAW) potentials describe the ion cores; exchange and correlation terms are described via the Perdew–Burke–Ernzerh functional. All simulations apply a (6 x 6) graphene supercell with a vacuum layer of 15 Å. Kinetic energy cutoff for the wave functions in all the calculations is 500 eV. Brillouin zone sampling is done using the Monkhorst-Pack technique with a 5 x 5 x 1 grid for relaxation and a 9 x 9 x 1 grid for density of states calculations. Structures were relaxed until the force on each atom was smaller than 0.02 eV/A. Binding energy E_B is defined with the expression:

$$E_B = E_{m-g} - E_g - E_m$$

where E_{m-g}, $-E_g$ and E_m are energies of the adsorbate on modified-graphene full system, the free-standing modified graphene, and the metal adatom, respectively. Charge transfer between adatom and graphene are visualized via charge density difference plots using VESTA 3 software.[121] Charge difference is defined via the expression:

$$\Delta n(r) = n_{m-g}(r) - n_g(r) - n_m(r)$$

where n_{m-g}, $-n_g$ and n_m are charge densities of the adsorbate on modified-graphene full system, the free-standing modified graphene, and the metal adatom, respectively.

Finally, nudged elastic band (NEB) measurements were performed using VASP Transition State Theory (VTST) tools developed by Jónsson et. al. [122,123] and maintained by Henkelman et. al.[124–126]

5.3 Establishing Binding Sites on Graphene Surfaces

First, in this work, stable atomic arrangements and electronic structures of small ensembles of Pt atoms are investigated on pristine graphene surfaces and those modified with vacancy defects and dopants. All geometric optimizations and electronic structure calculations have been carried out through the spin-polarized density functional theory (DFT) calculations as implemented in the Vienna ab initio simulation package (VASP).[48,94,120] The systems investigated are shown in Figure 13, specifically (a) Pt_n clusters (n = 1,2,3) relaxed in vacuum and the substrate supports that include (b) pristine graphene (PG), (c) single vacancy graphene (SVG), and (d) pyridinic nitrogen-doped graphene (PNG). In the last case, a carbon double vacancy in the graphene lattice reconstructs in the presence of a nitrogen dopant, breaking the 6-fold lattice symmetry and forming a "pyridinic nitrogen" configuration of 6 and 5 element rings. This last structure is commonly observed in scanning tunneling microscopy (STM) investigations of nitrogen-doped graphene systems.[127–129] When examining variations in catalytic activity as a function of Pt cluster size and electronic structure of graphene supports, it is also important to investigate the stability of clusters from trimers down to a single Pt atom on graphene. The most efficient use of Pt would be to stabilize a single atom with high catalytic activity.

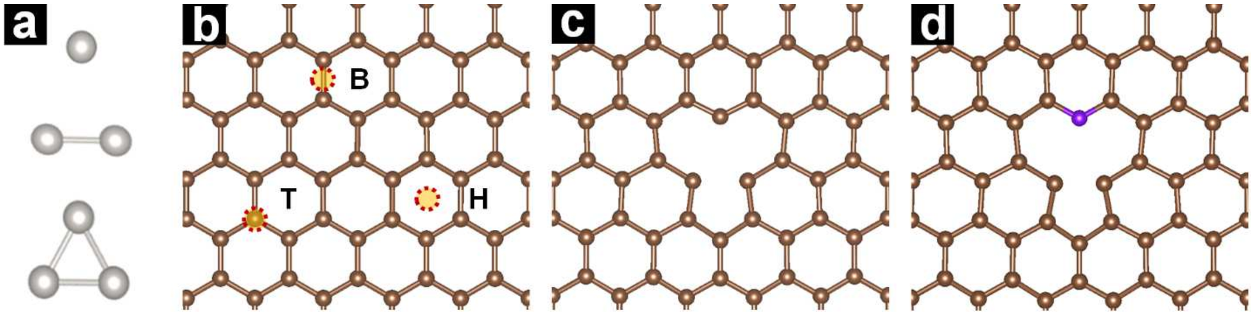

Figure 13: Optimized DFT models of: (a) platinum clusters of 1, 2, and 3 atoms in size relaxed in vacuum; (b) pristine graphene; (c) single vacancy graphene; (d) pyridinic N-doped graphene

One of the major roadblocks in implementing single atom catalysis is that even if single atoms are deposited on a substrate, these isolated atoms often prefer to migrate on the surface and eventually aggregate into clusters.[118,119] The potential of migration and cluster formation must be addressed in order to assess the true viability of single atom catalysis. The methods presented here attend to this issue by considering cluster formation via interaction between nearby Pt, each at neighboring stable sites. In the case of a single adatom on PG, there are three possible adsorption sites: top (directly sitting above a carbon atom), bridge (located above a carbon-carbon bond), and hollow (which is at the center of a hexagon in the carbon honeycomb lattice). These sites are highlighted in Figure 13b and labelled B, T, and H, respectively. Binding energies (E_B) are calculated to characterize the stability of Pt at sites of interest on the graphene substrates and demonstrate that the most stable position for a Pt adatom is at the bridge site, shown in Figure 14a, having an E_B of -1.53 eV and a $d_{Pt\text{-}C}$ of 2.1 Å, which is in accordance with previous reports.[61,130–132] The top site is nearly just as favorable, with an E_B of -1.69 eV, and the energy barrier for Pt to migrate between two neighboring bridge sites by passing through a metastable top site is determined to be only 0.16 eV. At room temperature, this corresponds roughly to a Pt atom hopping 20 times every second,[133] which means that Pt migration must be accounted for in any practical implementations.

Therefore, to evaluate the stability of a single atom, one must compare the E_B of adding adatoms to form a larger cluster with that of a single adatom. The evaluation of determining if there is a preference for forming a Pt dimer begins with the optimized single atom configuration and considers all symmetrically equivalent neighboring stable sites (top and bridge) in the honeycomb lattice as well as the site directly atop the original Pt atom as viable locations to add a second Pt atom. For trimers, this process is repeated on the optimized dimer configuration.

When considering two Pt atoms, the E_B and distance to the substrate both increase to -2.19 eV and 2.22 A, respectively, suggesting that the increase in E_B results from Pt-Pt interaction rather than Pt-C interaction. The addition of a third Pt atom further increases the E_B of the overall cluster to -2.88 eV/atom while the Pt-C distance remains the same (2.22 Å). These findings are summarized in Table 1 and in accordance with the literature [130–132] and indicate that Pt prefers to cluster on PG and is stabilized with interactions with other Pt atoms, rather than solely interacting with the graphene substrate as an isolated adatom. These results show PG is unsuitable for anchoring isolated Pt and facilitating single atom catalysis; more importantly, they establish a methodology useful in evaluating other substrates.

	Pt_1		Pt_2		Pt_3	
	E_B	d_{Pt-C}	E_B	d_{Pt-C}	E_B	d_{Pt-C}
PG	-1.53 eV	2.10 Å	-2.19 eV	2.22 Å	-2.88 eV	2.22 Å
SVG	-7.10 eV	1.94 Å	-5.36 eV	1.95 Å	-4.82 eV	1.97 Å
PNG	-4.89 eV	1.94 Å	-4.31 eV	1.96 Å	-4.14 eV	1.98 Å

Table 3: Binding energies and Pt-C distance for Pt_n clusters PG, SVG, and PNG.

5.4 Single Vacancy Graphene

Conversely, this methodology affirms the potential of SVG as a support structure for single Pt atoms, so long as there is a high enough vacancy density on the surface such that every Pt atom can be accommodated. Indeed, SVG substrates have been observed in the literature to support catalytically active metal nanoclusters.[134,135] The trapping ability of that vacant site for the SVG system is reflected in the large E_B, -7.10 eV. Charge density difference plots provide insight into this high E_B by observing the spatial redistribution of charge density as an adsorbate binds to a substrate surface by subtracting the superposition of the respective charge densities of the individual adsorbate and the substrate. As shown in Figure 15, the presence of vacancy defects in the graphene honeycomb lattice provides dangling bonds which induce charge on adjacent C atoms and influence these electron deficient atoms to stabilize themselves by bonding with Pt. For a single Pt atom on SVG, the adsorbate binds to the vacant site, shifting out of plane from the honeycomb lattice by a height of 1.03 Å due the atom's size mismatch.[60,62,136] Upon increasing the cluster size to two or three atoms, a single Pt atom anchors the rest of the cluster at the defect site and d_{Pt-C} hardly changes. For the dimer and trimer Pt, the E_B

decreases to -5.36 and -4.82 eV, respectively. These values, shown in **Error! Reference source not found.**, are in accordance with that from the literature [135] and suggest that Pt atoms would each prefer to find separate vacancy sites rather than cluster together at one vacancy site, explaining the stability of Pt_1/SVG.

It is important to note that ability to isolate Pt atoms on SVG is coverage dependent.[137] If the number of graphene vacancies is less than the number deposited Pt atoms, then clustering will occur. In the calculations presented here, the graphene cell size is (6x6), simulating one defect per 71 C atoms and an atomic ratio of roughly 3% and 4% Pt to C for the dimer and trimer cluster, respectively. Results suggest that an atomic ration of ≤1.4% Pt to C must be maintained in order to preserve the isolation of Pt atoms (see Supplementary Information for further detail).

When examining potential for promoting chemical reactions of this Pt_1/SVG system, density of states (DOS) plots allow for the comparison of electronic structures between new systems of interest and well-established catalysts. For example, Pt is a well-known catalyst often used for industrial applications; yet, an abundant amount of research has shown that only atomic sites of specific coordination participate in enhancing reactions. [138–140] In the search for the ideal single atom Pt catalyst, it is therefore important to recreate the electronic structure of these useful sites. As observed in Figure 15, the broadened Pt states overlap with the total DOS lying around the Fermi energy, an indication of strong hybridization between the Pt and the neighboring C atom.[141] The d-orbitals of the Pt atom provide occupied states 0.46 eV below the Fermi energy, which other studies have shown allows for weak CO adsorption and facilitates the O_2 adsorption, enhancing the catalytic activity for CO oxidation and methanol oxidation.[105, 63]

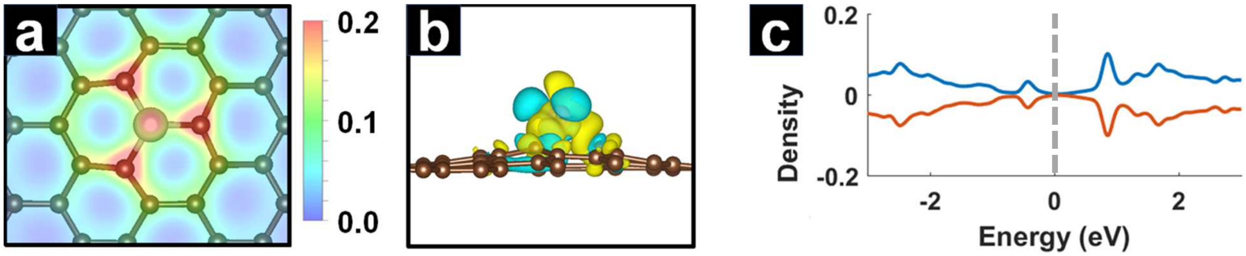

Figure 15: Charge maps (a), charge density difference plots (b), and DOS plots (c) for a Pt atom adsorbed on SVG. The charge maps are plotted in units of e/Bohr^3. In the charge density difference plots, yellow and blue represent charge accumulation and depletion, respectively. The DOS plots reflect the number of states/eV for the total DOS of the system, where the Fermi level is set to 0 eV.

5.5 Pyridinic N-doped Graphene

Although there are numerous theoretical studies exploring properties of Pt on PG, SVG, and N-doped graphene surfaces, adatom properties on N-doped pyridinic configuration has been less explored.[142,143] Surprisingly, PNG is the structure commonly observed in STM investigations of nitrogen-doped graphene systems.[127–129] Furthermore, X-ray photoelectron spectroscopy studies have identified PNG as highly catalytically active.[144,145] It has been reported that the presence of pyridinic-N influences the local electronic structure, increasing the density of π states near the Fermi level and lowering the work function.[146] For these reasons, PNG is a promising substrate to consider for single Pt atom catalysis, and results here show that it is also a suitable candidate for stabilizing the single Pt atom. As shown in **Table 1**, the addition of Pt atoms decreases E_B and increases $d_{Pt\text{-}C}$. Rather than clustering, the Pt atoms prefer to distribute themselves amongst separate PNG sites.

For PNG, the nitrogen contributes more than is reciprocated by the adjacent carbons, which use an sp3-hybridized orbital to bond with the N atom due to the resulting underutilization of its 2pz orbital.[147] In the case of Pt_1/PNG, the N and Pt insert themselves into the two carbon vacancies, sinking in plane and reforming the honeycomb lattice. As seen in Figure 16 a and b, excess charge from the nitrogen weakly interacts with the Pt, which instead strongly attracts to the dangling bonds of the neighboring carbons. resulting in an E_B of 4.89 eV. Although this value lower than that for the SVG case, the $d_{Pt\text{-}C}$ bond length is the same for both supports, indicating the favorability of reconstructing the honeycomb lattice.

The addition of the dopant N atom strongly influences the electronic structure, which deviates greatly from that for SVG. The resulting system is magnetic with occupied states on the down spin 0.15 eV below the Fermi level and on the up spin 0.31 eV above the Fermi level (Figure 16 c). These occupied states and the spin splitting are unique, and combined with the high stability of the isolated Pt atom, make the Pt/PNG system an interesting system to investigate for potential catalytic activity.

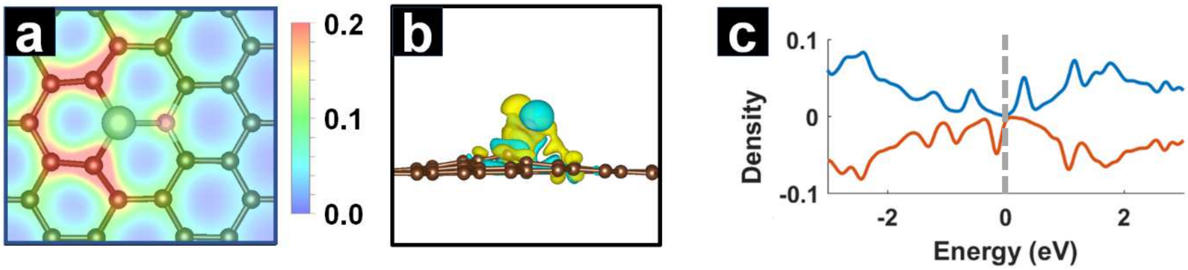

Figure 16: Charge maps (a), charge density difference plots (b), and density of states plots (c) for a platinum atom adsorbed on pyridinic N-doped graphene. The charge maps are plotted in units of e/Bohr3. In the charge density difference plots, yellow and blue represent charge accumulation and depletion, respectively.

5.6 Investigations of Chemical Activity

The catalytic activity of Pt/PNG has already been demonstrated for the hydrogen evolution reaction in which H_2 dissociates through charge donation via the Pt atom.[148]

Additionally, results here suggest that the Pt/PNG system is also catalytically active for the oxidation of CO into CO_2. For this optimized structure of Pt_1/PNG system, the adsorption geometry and the energetics of the following gas molecules were investigated H_2, O_2, H_2O, CO, and CO_2. The study of these molecules facilitates the investigation of hydrogen evolution and carbon monoxide oxidation reactions, which are chosen for their simplicity and popularity in the literature.[97,149] Minimizing the total energy, the most stable adsorption geometry of each gas molecule on the single Pt adatom was determined. Similar gas adsorption studies have been previously performed for Pt/SVG.[63,150] In this work, the Pt/PNG system is specifically of interest. The binding energies of each these molecules are summarized in Table 4, where the binding energy E_{ads} is defined as

$$E_{ads} = E(g/Pt/PNG) - E(g) - n \times E(Pt/PNG)$$

Where n represents the number of platinum adsorbate atoms in the system and $E(g/Pt/PNG)$, $E(g)$ and $E(Pt/PNG)$ are energies of the gas molecules adsorbed on Pt/PNG, the free gas molecule in vacuum, and the Pt/PNG system, respectively.

	Binding Energy (eV)
H_2	-1.484
O_2	-1.533
H_2O	-0.345
CO	-1.819
CO_2	-0.559

Table 4: Binding energies of molecules to Pt/PNG.

Many adsorption sites were tested to determine the most stable configuration for each adsorbate. Comparing these energy values reveals that the Eads for CO and O_2 is relatively high compared to that for CO_2, which suggests the possible enhancement CO to CO_2 conversion. CO and O_2 molecules adsorb about 2 Å away from the Pt atom. After adsorbtion, the C−O bond length is almost the same as that of an isolated CO molecule in vacuum; in contrast, as shown in Figure 17a, O_2 adsorbs to the Pt atom parallel to the plane of the graphene. E_{ads} is 1.53 eV, and charge is donated to the molecule, increasing the bond length from 1.24 Å to 1.44 Å. This elongation occurs due to the electronic charge transfer from the Pt atom to the $2\pi^*$ orbital of O_2. However, from the energetic point of view, adsorption of the CO molecule to Pt_1/PNG is preferred over that of the O_2 molecule.

These energy and length values are similar to that for Pt/SVG, a system which has been predicted to catalyze CO oxidation via the Langmuir–Hinshelwood mechanism.[63] It would therefore be interesting to see if Pt/PNG can also facilitate this reaction. The limiting step in the reaction is the dissociation of the oxygen dimer, which is found here to have a prohibitively high dissociation energy of 6.66 eV, in accordance with the literature.[151] However, in weakening the O_2 bond, this dissociation energy is decreased to in the presence of the Pt_1/PNG catalyst. The CO oxidation reaction pathway may be traced using the nudged elastic band method, as shown in Figure 17b. The initial state (IS) is composed of a CO molecule in the presence of O_2 adsorbed to the Pt_1/PNG. Throughout the reaction, one of the oxygen atoms begins approaching the carbon atom of CO, eventually forming the transition state (TS) with an energy barrier of 0.36 eV, where the O—O bond is elongated to 1.67 Å and a peroxo-type O–O–C–O complex is formed over the Pt atom. Afterward, the O—O bond dissociates entirely, allowing the CO_2 molecule to release entirely, which drops the energy of the system by 3.49 eV. The 0.36 energy barrier for the reaction is a modest one and comparable to the 0.31eV energy barrier determined for the Pt_1/SVG system.

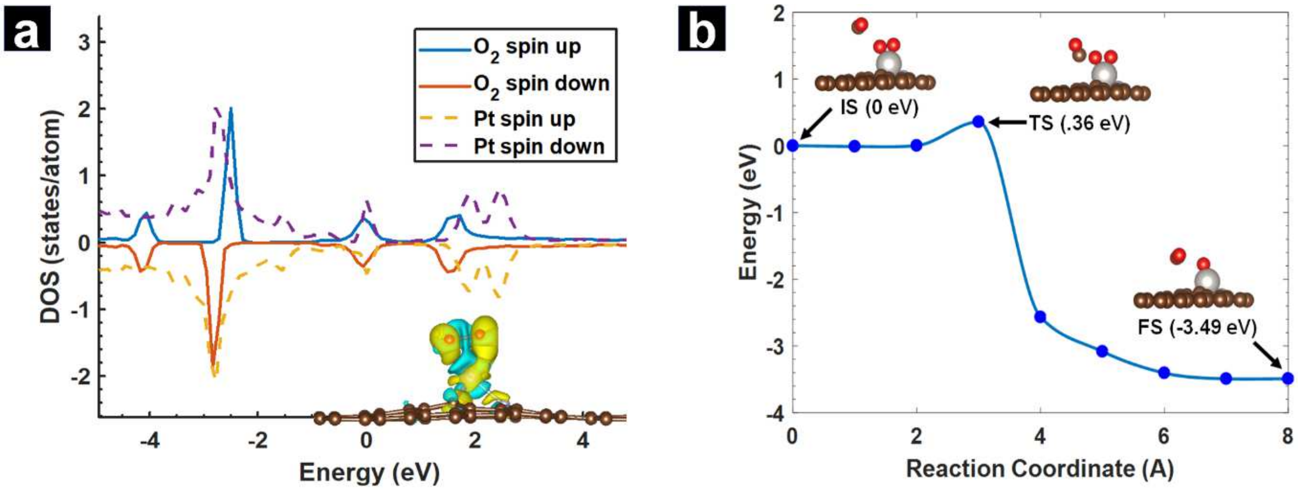

Figure 17: a) The density of states projected for different atoms are found with the Fermi level (placed at 0 eV) for Pt1/PNG. b) Optimized structures of CO oxidation on the Pt1/PNG demonstrate the LH reaction including the initial state (IS), transition state (TS), and final state (FS). Red, brown, and white balls represent oxygen, carbon and Pt atoms, respectively.

5.7 Conclusion

DFT methods have been applied to investigate the feasibility and catalytic activity of single atom Pt on pristine, defected, and doped supports. The different graphene substrates can influence the stability of the single Pt atom, modify its electronic structure, and result in varying catalytic activities. This work has identified a novel catalyst consisting of a single Pt atom on pyridinic N-doped support. The Pt–C covalent bonding of the adsorbed Pt atom at the vacant site of the honeycomb lattice is responsible for the strong binding and stabilization of the single Pt atom on the PNG substrate. The Pt/PNG exhibits high catalytic activity for CO oxidation with a modest energy barrier of 0.36 eV. Compared to other support system such as carbon sheets, the Pt/PNG system offers itself as a prime candidate for atomic scale catalysis, specifically CO oxidation, providing a new alternative for lower cost and higher efficiency reactions as well demonstrating the tunability of defected graphene as a support structure for catalysis.

CHAPTER 6: Bijel-templated 3D Graphene Architectures

Graphene is an atomically thin material composed solely of carbon, and it exhibits excellent properties such as high electrical and thermal conductivities, large specific surface area, and excellent stability.[152–154] Furthermore, graphene's flexible two-dimensional geometry and high mechanical strength allows for the creation of free-standing structures with high surface area such as graphene nanotube networks, foams, and aerogels.[155–160] Such structures are promising for applications such as electrochemical energy storage, hydrogen storage, catalysts and the creation of meta-materials; even so, many three-dimensional graphene (3DG) systems are randomly constructed architectures, which suffer from reduced analyte flow due to tortuous transport, blocked channels, or otherwise inaccessible geometries that can negatively affect the originally promising characteristics.[161] Various attempts have been made to overcome these issues, but each come with their own drawbacks. While photolithography offers great control over 3DG structures with regular patterns of various geometrical shapes, the complexity of the lithography techniques required limits the throughput of such structures to thin layers of <50 μm.[162] The use of dealloyed metals has produced porous graphene with 0.1 – 2 μm pores,[163] and commercial metal foams easily produces pore sizes in the hundreds of μm.[164–166] However, controlled pore distributions between 1-100 μm has not been reliably demonstrated; as an example, Li et. al. demonstrated controlled pore sizes <100 μm but the original morphology could not be preserved for the final freestanding graphene system.[158]

The use of bicontinuous interfacially jammed emulsion gels (bijels) may provide a pathway to addresses many of these issues. Bijels are soft materials formed through arrested spinodal decomposition of a ternary liquid-liquid-colloid mixture; they are notable for their node-free open-pore morphologies and tunable pore size distributions,[167,168] resulting in an internal macrostructure composed of kink-free pathways.[169–172] Moreover, the self-assembly of bijels naturally forms a minimal surface area geometry with uniform domain size, negative Gaussian curvature, and vanishing mean curvature, resulting in an internal architecture that is predominantly composed of saddle points at the internal surface sites.[173] The work herein applies a bottom-up fabrication approach using bijels as sacrificial templates for nickel deposition and subsequent chemical vapor deposition (CVD) growth of graphene. Upon removing the nickel backbone, the final product is a freestanding bicontinuous macroporous 3DG (Bi-3DG) with properties characteristic of both bijels and graphene. To our knowledge, these structures are the first implementation of graphene into a minimal surface area geometry.

6.1 Fabrication of Bi-3DG

Bicontinuous three-dimensional multilayer graphene architectures (Bi-3DG) are fabricated using chemical vapor deposition (CVD) of methane on a sacrificial Ni scaffold. The Ni scaffold is formed via electroless deposition of Ni on a polyethylene (glycol) diacrylate (PEGDA) bijel-derived template, which provides the porous bicontinous 3D architecture. Bijels are formed by jamming of colloidal silica particles (500 nm diameter) at the interface between immiscible water and 2,6-Lutidine phases under conditions where spinodal decomposition occurs. PEGDA templates are derived by infusing the mixture with a photoactive monomer (PEGDA) that preferentially mixes with 2,6-Lutidine, followed by UV exposure to polymerize PEGDA. The remaining liquid phases are drained and silica particles are removed with hydrofluoric acid. Electroless deposition of Ni in a 20 mM nickel chloride hexahydrate plating solution for 75 minutes produces a Ni coating with an approximate thickness of 1 µm throughout the bijel template.[174]

The Ni/PEGDA template is subsequently sintered for 4 hours at 300°C and 4 hours at 500°C in air to remove PEGDA and then annealed at 450°C for 8 hours in a reducing environment of 10% H_2 in Ar, resulting in a metallic Ni scaffold. In the next processing stage, CVD is performed at 900°C in a tube furnace with methane as a precursor to grow graphene on the Ni scaffold.[175–177] Finally, the Ni backbone is etched in a 1M solution of $FeCl_3$ to produce a free-standing Bi-3DG. Figure 18 a-d shows the schematic of the growth steps alongside optical images of the (a) PEGDA template, Ni scaffold (b) before and (c) after CVD, and finally (d) the Bi-3DG alongside a ruler to show the macroscopic length scales.

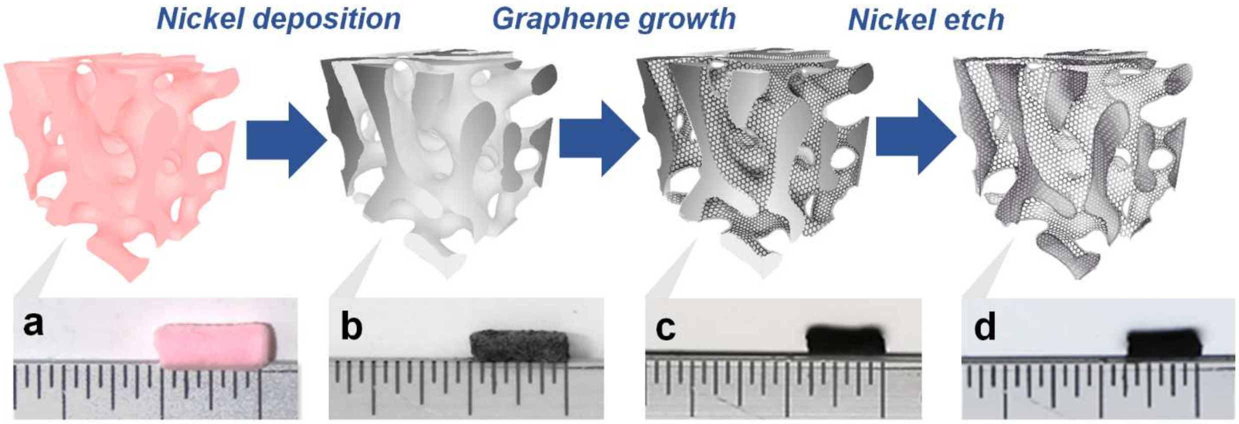

Figure 18: Schematic depicting the Bi-3DG synthesis process. (a) A PEGDA bijel template is (b) coated with a Ni film via electroless deposition. The Ni/PEGDA bijel template is sintered/reduced and then used as a scaffold for (c) CVD graphene growth. Finally, the (d) Ni backbone is etched away in an FeCl3 solution. Below each schematic, an optical image of the macroscopic structure is shown alongside a ruler. The bijel template length in (a) is 0.25 inches.

SEM images, as shown in Figure 19**Error! Reference source not found.** a-c for the stages of Ni deposition, CVD growth, and Ni etch, respectfully, confirms the preservation of the bicontinuous morphology with approximately 30 μm sized pores and demonstrates the capability to grow graphene-based bijel structures. A red circle in the images highlights the same feature on the surface to indicate the images were acquired in the same region. Due to difficulties in mounting the non-planar sample, SEM images show changes in perspective due to tilt/rotation of the sample itself.

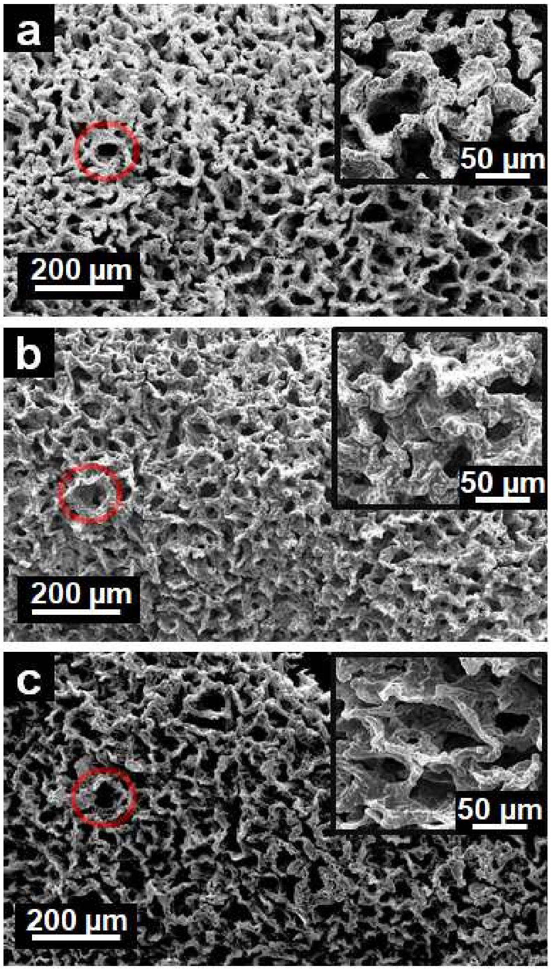

Figure 19: SEM images of a bijel-templated sample (a) after sinter and reduction of electrolessly-plated Ni, (b) after CVD growth of graphene at 900°C on Ni scaffold, and (c) after FeCl3 etch of Ni to form Bi-3DG structure.

To track the compositional changes in the system after each stage of synthesis, chemical analysis is conducted using XPS. As shown in Figure 20 a, the signature Ni 2p peak at 852.6 eV is observed after electroless deposition and remains after CVD growth. The Ni

2p peak is not observed after etching in $FeCl_3$, which is the step used to remove the Ni scaffold. XPS spectra in the region of the C 1s peak is shown in Figure 20 b. A small C 1s peak is observed before CVD graphene growth is performed, likely due to residual C remaining from the PEGDA template after the sintering step. Unsurprisingly, the C 1s signal increases after CVD growth. The location of the C 1s peak location shifts closer to 284 eV after CVD growth and is consistent with sp2-hybridized (graphitic) carbon.[178]

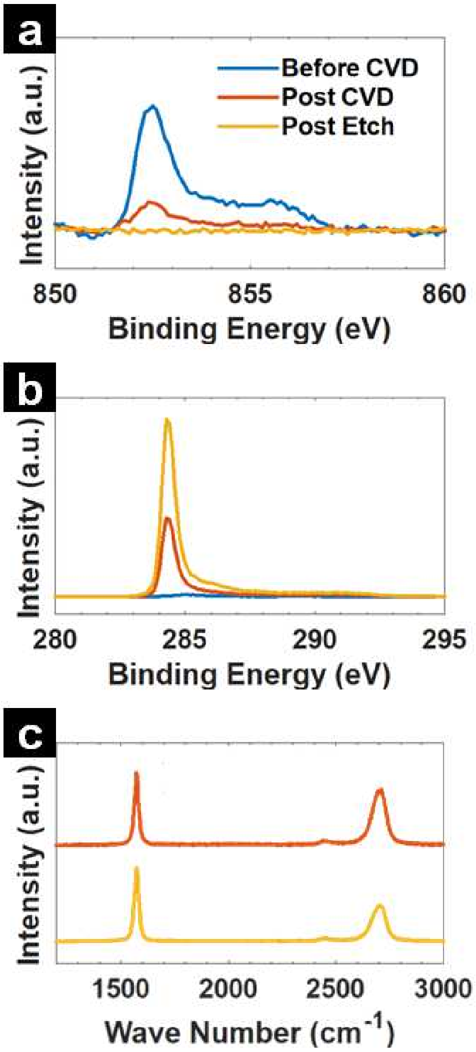

Figure 20: XPS spectra of the (a) Ni 2p peak and (b) C 1s peak on the Ni scaffold (blue curve), after CVD growth (red curve), and forming a Bi-3DG after FeCl3 etch (gold curve). Representative Raman spectra (c) taken after CVD growth (red) and etch (gold).

However, to better confirm the presence of graphene, measure its quantity, and asses its quality, Raman spectroscopy measurements were also performed after CVD growth as well as after etch in $FeCl_3$ to further assess the chemical environment of C in the 3D structure. The data is plotted in Figure 3c and the two most intense features observed are located at the 1580 cm^{-1} and the 2700 cm^{-1}, referred to as the G band and 2D band, respectively. It is generally understood that the intensity ratio 2D/G qualitatively gauges the extent of layer-layer interaction in graphene systems.[179] For instance, as the number of graphene layers in a system increases this intensity ratio decreases, with the exception that turbostratic graphite displays a high intensity ratio despite its multilayer nature due to rotational disorder decreasing the interlayer coupling[180–182]. To lend more insight into the stacking order, it is useful to look toward the shape of the 2D peak as well. With additional layers, the 2D peak broadens, and turbostratic graphite displays a 2D full-width at half maximum (FWHM) that is approximately double that of single-layer graphene[181,182]. By analyzing changes in both the width of the 2D peak and the 2D/G intensity ratio, we compare the quality of graphene films at different processing stages.

Raman spectra were taken at approximately 30 distinct points on each sample, and histograms for the measured 2D FWHM and the 2D/G ratio are shown in Figure 21. It is seen that the graphene film on the Ni scaffold (a and b) displays a broad range of values for the 2D FWHM, from 20 cm^{-1} to 70 cm^{-1}, and similarly there is a broad distribution of intensity ratios between 0.1 and 3. These findings are consistent with spatial variations in the stacking behavior of the graphene films produced on Ni substrates.[183] The number of counts with a FWHM near 60 cm^{-1} implies the presence of many rotationally misaligned graphene sheets, whose weak interlayer coupling is also reflected in the intensity ratio histogram where we see the distribution centered near 1 rather than the lower intensity ratio we would expect from closely-stacked multi-layer graphene.

Figure 21 c and d show the 2D FWHM and intensity ratio for the system after etching the Ni backbone away. The distribution become much sharper around the peak at 60 cm^{-1} which indicates a higher degree of spatial uniformity. The smaller peak remains at 35 cm^{-1}, which is consistent with the presence of regions with a large mismatch angle between graphene layers.[184] The general decrease in counts with low 2D FWHM shows that the graphene films are, in general, stacking more closely, and there are fewer points that resemble freestanding graphene (i.e. with a FWHM near 20 cm^{-1} and a high intensity ratio). This is supported by the intensity ratio histogram, which shows a clear decrease in the average intensity ratio. This change in stacking is attributable to the removal of the rigid support, since its removal allows the graphene layers to relax and settle more freely.

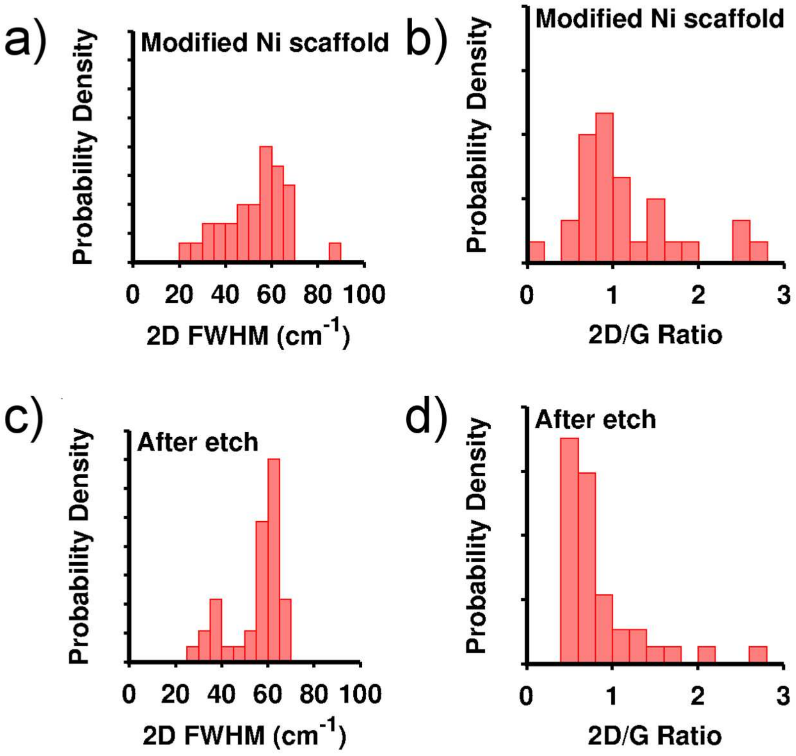

Figure 21: Probability density histograms showing results of Raman spectrum analysis. The measured values for the 2D peak FWHM and the intensity ratio I2D/IG are shown for (a and b) the graphene-modified Ni scaffold and (c and d) Bi-3DG.

In order to examine the atomic structure of the Bi-3DG system via scanning tunneling microscopy (STM), two-dimensional analogues (2DG) were produced using electroless deposition of 1μm thick Ni films onto modified SiO_2 surfaces followed by CVD graphene growth. Figure 22 a and b show low-voltage SEM images after CVD growth on a 3D and 2D sample respectively, respectively. Ni grains in the size range of 1μm - 5μm are observed in both images. Additionally, regions of various contrasts are visible, and previous studies have suggestedthese regions may correspond to different graphene domains.[185] As shown in Figure 22 c, Raman measurements of the Bi-3DG and 2DG exhibit similar spectra. These spectra resemble single-layer graphene with their low FWHMs and high intensity ratios, but single-layer graphene should interact strongly with the Ni substrate and suppress the signature graphene modes. [183] Histograms showing the trends for the 2D FWHM and intensity ratio as measured using Raman spectroscopy are shown in the Supplementary Information. Variations in the spectra correspond to varying degrees of interlayer coupling due to rotational misalignment and geometrical variations, and are not purely due to variations in layer number. [186,187] Overall, these histograms resemble the Bi-3DG system (after the Ni scaffold is etched), with a FWHM distribution centered near 60 cm^{-1}, and a 2D/G intensity ratio distribution centered near 0.6. The similarity between the two sets of histograms indicates that the 2D system has graphene layers that are already stacked in an energetically favorable fashion; they do not need the removal of the rigid substrate to relax their structure. These histograms indicate that the 2DG is a simplified system which has graphene films that resemble that of Bi-3DG.

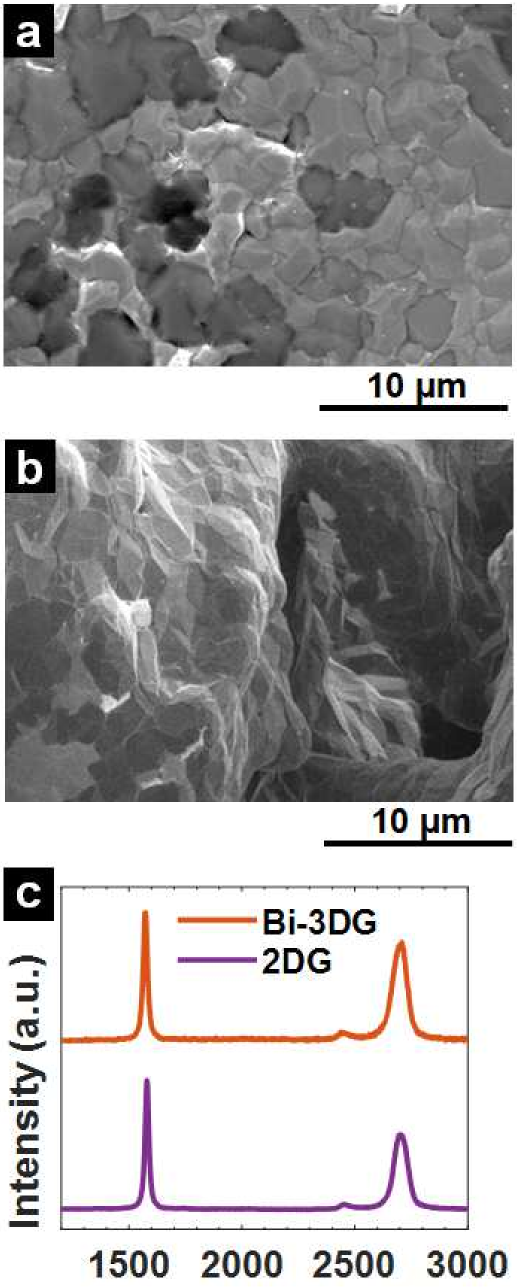

Figure 22: (a,b) Low voltage SEM image of Bi-3DG and 2DG after graphene growth. (c) Average of Raman spectroscopy maps taken for both the 2DG analogue and Ni-Bi-3DG show comparable intensity ratios between I2D and IG peaks.

When 2DG is characterized with STM, various Moiré patterns are visible on the surface. A typical STM image is shown in Figure 23, in which regions with three different Moiré patterns are highlighted in white boxes (labeled a,b, and c) and Fourier transforms of these three regions reveal bright spots indicative of low frequency periodicity. The large domain (Figure 23 b) exhibits two different Moiré patterns in its Fourier transform, which suggest an incommensurability with regards to two rotationally different graphene domains, both of which exist immediately below the uppermost surface layer. The Moiré pattern for Figure 23 a represents another graphene domain that is rotationally distinct from its neighbor, and a clear defect boundary demarks the transition from one domain into the other. The variety of rotational domains observed suggests decoupling between the graphene layers in the system. Additional faint boundaries can be seen in the large domain, suggesting the presence of deeper sub-surface graphene layers. Although it is uncertain how deep these layers are, the fact that the visible Moiré patterns appear independent of these boundaries suggests that overall, the graphene layers are decoupled from each other and the nickel film, resulting in pseudo-freestanding graphene.

These findings are consistent with that of similar studies that investigated the growth behavior of graphene on polycrystalline Ni.[188] Domains of polycrystalline Ni are randomly oriented on the macroscopic scale, and some possess the same facets as Ni(111). During CVD, the formation of graphene is inhomogeneous over a surface, because of the competing mechanisms of Ni(111) surface-catalyzed growth,[189] diffusion of C atoms into the bulk Ni, segregation of C to the surface, and graphene nucleation at the grain boundaries where different crystal orientations with different segregation abilities coexist. As such, graphene grains may connect with or grow over each other, resulting in multilayer graphene with rotational disorder and weak interlayer interactions in the final system.

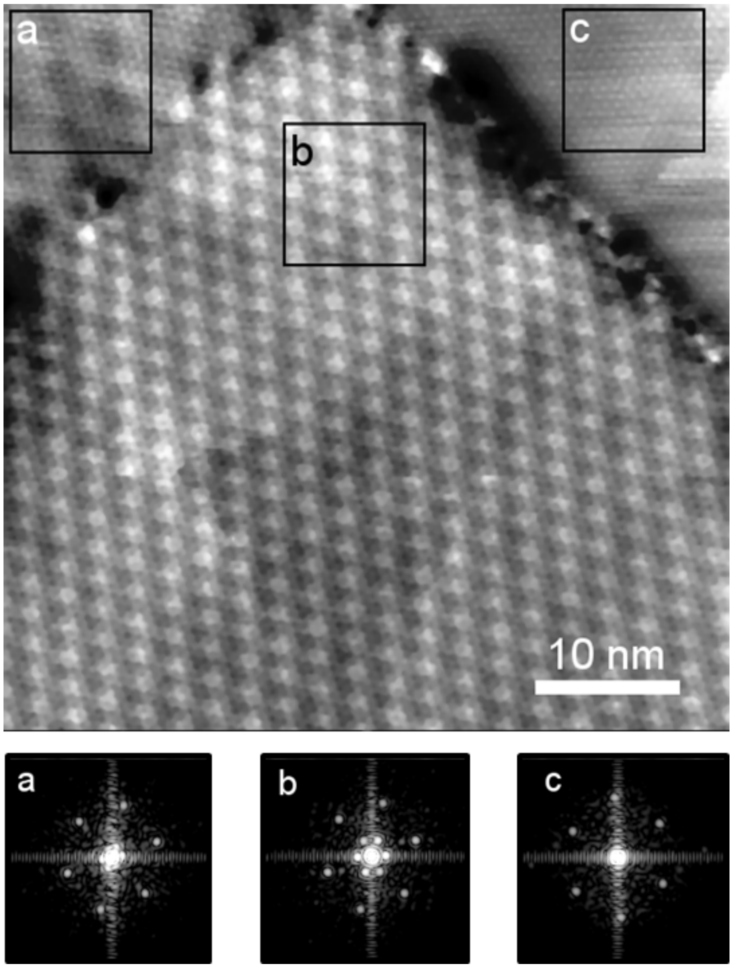

Figure 23: 50 nm X 50 nm STM image of a 2DG analogue (Iset = 0.4 nA, VGAP = 400 mV) of graphene on EN. Fourier transforms are taken in three regions displaying different Moire patterns.

6.2 Combining promising material and structural properties

The main promise of Bi-3DG lies in the ability to combine the favorable material properties of graphene with the favorable structural properties of the bijel's minimal surface area geometry.

For porous structures, surface area generally increases with a reduction in pore size. Compared to similarly-sized macroporous materials , bijels exhibit relatively high surface areas due to the accessibility of their interconnected pathways, and this value should increase for Bi-3DG. In general, carbon materials with high SSA are desired in applications such as the development of next-generation batteries or hydrogen storage.[190,191] The BET method using N_2 adsorption was utilized to measure specific surface areas (SSA). Results determined SSAs of 6.42 m^2/g before CVD growth, 14.03 m^2/g after growth, and 526.60 m^2/g after $FeCl_3$ etching. The initial increase in SSA after CVD growth is attributed to the extra surface area of the multilayer graphene. The high SSA in the final Bi-3DG system indicates the successful synthesis of a high surface area light weight material with non-tortuous pathways derived from the bijel structure. The analysis also confirms that effects such as graphene re-stacking and pore collapse did not significantly reduce the accessible surface area.[192,193]

As another test of the synergistic nature of Bi-3DG, mechanical properties were evaluated through performing uniaxial compression on punchout sample (0.8 mm in diameter and 2.25 mm tall) whose density was measured to be a 119 mg/cm^3. Several loading cycles were used estimate roughly 4.9 MPa as Young's modulus, which was 5x higher than that for the PEGDA bijel.[194] The density to Young's modulus ratio, 3.9 $kPa \cdot cm^3/mg$, of the Bi-3DG is the high amongst the reported value for graphene foam architectures, attesting to the successful, synergistic incorporation of the graphene into bijel's architecture.[127,195–200]

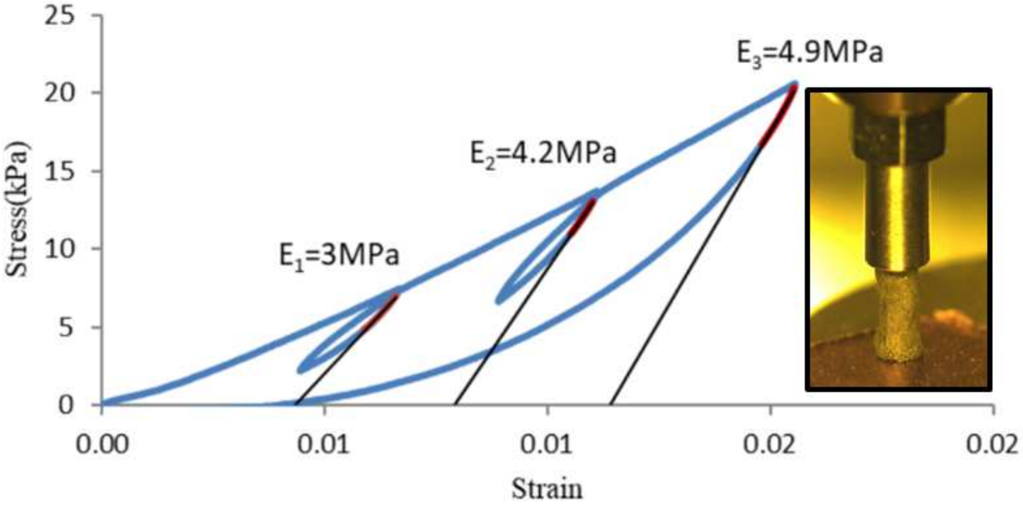

Figure 24: Strain vs. stress curve for the Bi-3DG sample under cyclic loading of incresing strain. The Young's modulus is measured to be about 4.9 MPa. Inset shows a picture of the test setup.

6.3 Conclusion

The work demonstrates the successful fabrication of Bi-3DG architectures through the use of bijels as sacrificial templates. SEM, XPS, Raman, and STM are used to characterize each fabrication step and confirm the successful incorporation of graphene into the bijel structure. The final product exhibits properties characteristic of both bijels and graphene, such as high surface area and high mechanical strength, as measured by the Young's modulus to density ratio. These characteristics make the Bi-3DG suitable at a stable catalytic support structure. Moreover, there is still room for improvement for the Bi-3DG, for example through the enhancement of the surface electronic structure via dopants or through development of higher quality graphene through the use of a metal alloy backbone during CVD growth.

CHAPTER 7: Conclusion and Future Work

From both a theoretical (DFT) and experimental (primarily STM) perspective, this thesis has explored aromatic carbon materials, starting with a small aromatic molecule, the PAH coronene, and ending with the largest aromatic crystal, graphene. Similar methods can be used to explore other PAH molecules; by looking at aromatic species of other sizes, it will be possible to determine the edge-mediated effects in a surface-dominated material. One route forward is to examine the surface morphology of other PAH molecules with known structures and compositions adsorbed on highly oriented pyrolytic graphene (HOPG). HOPG is chosen as a substrate to circumvent substrate mediated effects; because its chemical composition and planar structure are similar to that of the species of interest; HOPG should therefore exhibit similar interactions. Guiding experimental efforts, DFT calculations may be performed to provide image simulations, energy estimations, and interaction predictions. Directly observing and characterizing these PAH interactions will allow for the creation of a library of quantitative models to describe them.

Insight into the intermolecular interactions governing aromatic carbon species will foster the development of methods to tune these materials for various applications – including synthesizing higher quality graphene, controlling the fabrication of aromatic carbon into 3D structures (from nanoscale clusters to macroscale architectures), and mitigating nascent soot formation during engine combustion.

Appendix A: INCAR and KPOINT Files for DFT Calculations

INCAR 1:

```
ENCUT   = 500

# Ionic relaxation
EDIFF   = 1E-5  !  low accuracy
EDIFFG  = -0.02  !force

PREC = Normal
#PREC=Accurate
#NELM   = 100      !   maximum electronic steps
NELMIN  = 4         !  minimum electronic steps
#NELMDL  = -8     ! update of charge for 3 steps        (for continuation: 0)
IBRION  = 2        !  use CG algorithm for ions
NSW     = 1590    ! No. of steps for ion
#ISIF = 3
POTIM   = 0.2

AMIX = 0.1
BMIX = 0.0001 ! almost zero, but 0 will crash some versions
AMIX_MAG = 0.5
BMIX_MAG = 0.0001 ! almost zero, but 0 will crash some versions

#ALGO    = Fast    ! RMM-DIIS algorithm for electrons
#LREAL   = .TRUE.       ! evaluate projection operators in real space
LREAL  =  Auto

NPAR   = 8
NSIM    = 4       ! blocked algorithm update, four bands a time
GGA     = PE      ! PBE

ISMEAR = 0
SIGMA = 0.2

ISPIN=2
```

KPOINTS 1:

```
44
 0
g
 1 1 1
 0 0 0
```

INCAR 2:

```
ENCUT   = 500
# Ionic relaxation
EDIFF   = 1E-5  !  low accuracy
EDIFFG  = -0.02  !force

PREC = Normal
#PREC=Accurate
#NELM   = 100      !   maximum electronic steps
NELMIN  = 4         !  minimum electronic steps
#NELMDL  = -8     ! update of charge for 3 steps        (for continuation: 0)
IBRION  = 2        !  use CG algorithm for ions
NSW     = 1590    ! No. of steps for ion
#ISIF = 3
POTIM   = 0.2

AMIX = 0.1
BMIX = 0.0001 ! almost zero, but 0 will crash some versions
AMIX_MAG = 0.5
BMIX_MAG = 0.0001 ! almost zero, but 0 will crash some versions

#ALGO    = Fast    ! RMM-DIIS algorithm for electrons
#LREAL   = .TRUE.       ! evaluate projection operators in real space
LREAL  =  Auto

NPAR   = 4
NSIM    = 4       ! blocked algorithm update, four bands a time
GGA     = PE      ! PBE

ISMEAR = 0
SIGMA = 0.2

ISPIN=2
ICHARG=1
```

KPOINTS 2:

```
44
 0
g
 3 3 1
 0 0 0
```

INCAR 3:

```
ENCUT   = 600
# Ionic relaxation
EDIFF   = 1E-7  !  low accuracy
EDIFFG  = -0.02  !force

PREC = Normal

NELMIN  = 4         !  minimum electronic steps

IBRION  = 2        !  use CG algorithm for ions
NSW     = 1590    ! No. of steps for ion

POTIM   = 0.2

AMIX = 0.1
BMIX = 0.0001 ! almost zero, but 0 will crash some versions
AMIX_MAG = 0.5
BMIX_MAG = 0.0001 ! almost zero, but 0 will crash some versions

LREAL  =  Auto

NPAR   = 8
NSIM    = 4       ! blocked algorithm update, four bands a time
GGA     = PE      ! PBE

LWAVE=.FALSE.

 LORBIT = 10       !to calculate TDOS and PDOS of each atom

   ISMEAR = 0
   SIGMA = 0.2

ISPIN=2
LWAVE=.FALSE.
```

KPOINTS 3:

```
44
 0
g
 9 9 1
 0 0 0
```

INCAR for generating CHGCAR files:

```
SYSTEM = CeO2:DOS  zuo Pd shi yong
ENCUT   = 500
# Ionic relaxation
EDIFF   = 1E-5  !  low accuracy
EDIFFG  = -0.02  !force

PREC = Normal
#PREC=Accurate
#NELM   = 100      !   maximum electronic steps
NELMIN  = 4         !  minimum electronic steps
#NELMDL  = -8     ! update of charge for 3 steps        (for continuation: 0)
#IBRION  = 2        !  use CG algorithm for ions
#NSW     = 1590    ! No. of steps for ion
#ISIF = 3
POTIM   = 0.2
NGXF = 192
NGYF = 192
NGZF = 196
AMIX = 0.1
BMIX = 0.0001 ! almost zero, but 0 will crash some versions
AMIX_MAG = 0.5
BMIX_MAG = 0.0001 ! almost zero, but 0 will crash some versions

#ALGO    = Fast    ! RMM-DIIS algorithm for electrons
#LREAL   = .TRUE.       ! evaluate projection operators in real space
LREAL  =  Auto

NPAR   = 8
NSIM    = 1       ! blocked algorithm update, four bands a time
GGA     = PE      ! PBE

LORBIT = 10       !to calculate TDOS and PDOS of each atom
   ISMEAR = 0
   SIGMA = 0.1

ISPIN=2
```

KPOINTS for generating CHGCAR files:

```
44
 0
g
 5 5 1
 0 0 0
```

INCAR for generating DOS:

```
ENCUT   = 500
# Ionic relaxation
EDIFF   = 1E-5  !  low accuracy
EDIFFG  = -0.02  !force

PREC = Normal
#PREC=Accurate
#NELM   = 100      !   maximum electronic steps
NELMIN  = 4         !  minimum electronic steps
#NELMDL  = -8     ! update of charge for 3 steps        (for continuation: 0)
#IBRION  = 2        !  use CG algorithm for ions
#NSW     = 1590    ! No. of steps for ion
#ISIF = 3
POTIM   = 0.2

MIX = 0.1
BMIX = 0.0001 ! almost zero, but 0 will crash some versions
AMIX_MAG = 0.5
BMIX_MAG = 0.0001 ! almost zero, but 0 will crash some versions

#ALGO    = Fast    ! RMM-DIIS algorithm for electrons
#LREAL   = .TRUE.       ! evaluate projection operators in real space
LREAL  =  Auto

NPAR   = 8
NSIM    = 1       ! blocked algorithm update, four bands a time
GGA     = PE      ! PBE

   ISMEAR = 0
   SIGMA = 0.1

ISPIN=2
```

KPOINTS for calculating DOS:

```
44
 0
g
 9 9 1
 0 0 0
```

References

(1) Liu, Z.; Zhou, X. *Graphene: Energy Storage and Conversion Applications*; CRC Press, 2014.

(2) Jonathan Clayden, N. G. *Organic Chemistry By Clayden, Greeves, Warren, And Wothers (OUP, 2000, 1503pp.) Complete With Cover, TOC, Charts.*

(3) Patrick, G. *Organic Chemistry: A Very Short Introduction*; Oxford University Press, 2017.

(4) Smith, J. D. T.; Draine, B. T.; Dale, D. A.; Moustakas, J.; R. C. Kennicutt, J.; Helou, G.; Armus, L.; H. Roussel; Sheth, K.; Bendo, G. J.; et al. The Mid-Infrared Spectrum of Star-Forming Galaxies: Global Properties of Polycyclic Aromatic Hydrocarbon Emission. *Astrophys. J.* **2007**, *656* (2), 770.

(5) Zhao, L.; Kaiser, R. I.; Xu, B.; Ablikim, U.; Ahmed, M.; Joshi, D.; Veber, G.; Fischer, F. R.; Mebel, A. M. Pyrene Synthesis in Circumstellar Envelopes and Its Role in the Formation of 2D Nanostructures. *Nat. Astron.* **2018**, *2* (5), 413–419.

(6) Hudgins, D. M.; Charles W. Bauschlicher, J.; Allamandola, L. J. Variations in the Peak Position of the 6.2 Mm Interstellar Emission Feature: A Tracer of N in the Interstellar Polycyclic Aromatic Hydrocarbon Population. *Astrophys. J.* **2005**, *632* (1), 316.

(7) Mulas, G.; Malloci, G.; Joblin, C.; Toublanc, D. Estimated IR and Phosphorescence Emission Fluxes for Specific Polycyclic Aromatic Hydrocarbons in the Red Rectangle. *Astron. Astrophys.* **2006**, *446* (2), 537–549.

(8) Ehrenfreund, P.; Rasmussen, S.; Cleaves, J.; Chen, L. Experimentally Tracing the Key Steps in the Origin of Life: The Aromatic World. *Astrobiology* **2006**, *6* (3), 490–520.

(9) Wallace, P. R. The Band Theory of Graphite. *Phys. Rev.* **1947**, *71* (9), 622–634.

(10) Peierls, R. Quelques propriétés typiques des corps solides. *Ann. Inst. Henri Poincaré* **1935**, *5* (3), 177–222.

(11) Novoselov, K. S.; Geim, A. K.; Morozov, S. V.; Jiang, D.; Zhang, Y.; Dubonos, S. V.; Grigorieva, I. V.; Firsov, A. A. Electric Field Effect in Atomically Thin Carbon Films. *Science* **2004**, *306* (5696), 666–669.

(12) The Nobel Prize in Physics 2010 https://www.nobelprize.org/nobel_prizes/physics/laureates/2010/ (accessed May 5, 2018).

(13) Geim, A. K. Graphene: Status and Prospects. *Science* **2009**, *324* (5934), 1530–1534.

(14) Zhang, Y.; Tan, Y.-W.; Stormer, H. L.; Kim, P. Experimental Observation of the Quantum Hall Effect and Berry's Phase in Graphene. *Nature* **2005**, *438* (7065), 201–204.

(15) Yan, Z.; Nika, D. L.; Balandin, A. A. Thermal Properties of Graphene and Few-Layer Graphene: Applications in Electronics. *IET Circuits Devices Amp Syst.* **2015**, *9* (1), 4–12.

(16) Ambrosi, A.; Pumera, M. Electrochemically Exfoliated Graphene and Graphene Oxide for Energy Storage and Electrochemistry Applications. *Chem. – Eur. J.* **2016**, *22* (1), 153–159.

(17) Samad, Y. A.; Li, Y.; Schiffer, A.; Alhassan, S. M.; Liao, K. Graphene Foam Developed with a Novel Two-Step Technique for Low and High Strains and Pressure-Sensing Applications. *Small* **2015**, *11* (20), 2380–2385.

(18) Li, X.; Feng, J.; Du, Y.; Bai, J.; Fan, H.; Zhang, H.; Peng, Y.; Li, F. One-Pot Synthesis of CoFe 2 O 4 /Graphene Oxide Hybrids and Their Conversion into FeCo/Graphene Hybrids for Lightweight and Highly Efficient Microwave Absorber. *J. Mater. Chem. A* **2015**, *3* (10), 5535–5546.

(19) Wicklein, B.; Kocjan, A.; Salazar-Alvarez, G.; Carosio, F.; Camino, G.; Antonietti, M.; Bergström, L. Thermally Insulating and Fire-Retardant Lightweight Anisotropic Foams Based on Nanocellulose and Graphene Oxide. *Nat. Nanotechnol.* **2015**, *10* (3), 277–283.

(20) Liu, Y.; Yu, L.; Ong, C. N.; Xie, J. Nitrogen-Doped Graphene Nanosheets as Reactive Water Purification Membranes. *Nano Res.* **2016**, *9* (7), 1983–1993.

(21) Binnig, G.; Rohrer, H. Scanning Tunneling Microscopy---from Birth to Adolescence. *Rev. Mod. Phys.* **1987**, *59* (3), 615–625.

(22) Binnig, G.; Rohrer, H. Scanning Tunneling Microscopy. *Surf. Sci.* **1983**, *126* (1), 236–244.

(23) Binnig, G.; Rohrer, H.; Gerber, C.; Weibel, E. Tunneling through a Controllable Vacuum Gap. *Appl. Phys. Lett.* **1982**, *40* (2), 178–180.

(24) Binnig, G.; Rohrer, H.; Gerber, C.; Weibel, E. Surface Studies by Scanning Tunneling Microscopy. *Phys. Rev. Lett.* **1982**, *49* (1), 57–61.

(25) Binnig, G.; Rohrer, H.; Gerber, C.; Weibel, E. 7 \ifmmode\times\else\texttimes\fi{} 7 Reconstruction on Si(111) Resolved in Real Space. *Phys. Rev. Lett.* **1983**, *50* (2), 120–123.

(26) The Nobel Prize in Physics 1986 https://www.nobelprize.org/nobel_prizes/physics/laureates/1986/ (accessed Apr 29, 2018).

(27) Tersoff, J.; Hamann, D. R. Theory and Application for the Scanning Tunneling Microscope. *Phys. Rev. Lett.* **1983**, *50* (25), 1998–2001.

(28) Bardeen, J. Tunnelling from a Many-Particle Point of View. *Phys. Rev. Lett.* **1961**, *6* (2), 57–59.

(29) The Nobel Prize in Chemistry 1918 https://www.nobelprize.org/nobel_prizes/chemistry/laureates/1918/ (accessed May 1, 2018).

(30) *CRC.Press.Handbook.of.Chemistry.and.Physics.85th.Ed.EBook LRN.*

(31) Lang, N. D. Vacuum Tunneling Current from an Adsorbed Atom. *Phys. Rev. Lett.* **1985**, *55* (26), 2925–2925.

(32) Selloni, A.; Carnevali, P.; Tosatti, E.; Chen, C. D. Voltage-Dependent Scanning-Tunneling Microscopy of a Crystal Surface: Graphite. *Phys. Rev. B* **1985**, *31* (4), 2602–2605.

(33) Ardenne, M. von. Das Elektronen-Rastermikroskop. *Z. Für Phys.* **1938**, *109* (9–10), 553–572.

(34) McMullan, D. Scanning Electron Microscopy 1928–1965. *Scanning* **1995**, *17* (3), 175–185.

(35) Goldstein, J.; Goldstein, J. I.; Newbury, D. E.; USA), D. E. (National I. of S. and T. N., Gaithersburg MD; Joy, D. C.; Echlin, P.; Lyman, C. E.; Lifshin, E.; Sawyer, L.; USA), C. E. (Lehigh U. L., Bethlehem PA; et al. *Scanning Electron Microscopy and X-Ray Microanalysis: Third Edition*; Springer US, 2003.

(36) Siegbahn, K.; Edvarson, K. β-Ray Spectroscopy in the Precision Range of 1 : 105. *Nucl. Phys.* **1956**, *1* (8), 137–159.

(37) Kai M. Siegbahn - Nobel Lecture: Electron Spectroscopy for Atoms, Molecules and Condensed Matter https://www.nobelprize.org/nobel_prizes/physics/laureates/1981/siegbahn-lecture.html (accessed May 1, 2018).

(38) Krishnan, R. S.; Shankar, R. K. Raman Effect: History of the Discovery. *J. Raman Spectrosc.* **1981**, *10* (1), 1–8.

(39) A New Type of Secondary Radiation : Abstract : Nature http://www.nature.com/nature/journal/v121/n3048/abs/121501c0.html (accessed Oct 11, 2017).

(40) Porto, S. P. S.; Wood, D. L. Ruby Optical Maser as a Raman Source. *J. Opt. Soc. Am.* **1962**, *52* (3), 251.

(41) Brunauer, S.; Emmett, P. H.; Teller, E. Adsorption of Gases in Multimolecular Layers. *J. Am. Chem. Soc.* **1938**, *60* (2), 309–319.

(42) Dollimore, D.; Spooner, P.; Turner, A. The Bet Method of Analysis of Gas Adsorption Data and Its Relevance to the Calculation of Surface Areas. *Surf. Technol.* **1976**, *4* (2), 121–160.

(43) The Nobel Prize in Chemistry 1998 https://www.nobelprize.org/nobel_prizes/chemistry/laureates/1998/ (accessed May 2, 2018).

(44) Segall, M. D.; Lindan, P. J. D.; Probert, M. J.; Pickard, C. J.; Hasnip, P. J.; Clark, S. J.; Payne, M. C. First-Principles Simulation: Ideas, Illustrations and the CASTEP Code. *J. Phys. Condens. Matter* **2002**, *14* (11), 2717.

(45) Hohenberg, P.; Kohn, W. Inhomogeneous Electron Gas. *Phys. Rev.* **1964**, *136* (3B), B864–B871.

(46) Phys. Rev. 140, A1133 (1965) - Self-Consistent Equations Including Exchange and Correlation Effects https://journals.aps.org/pr/abstract/10.1103/PhysRev.140.A1133 (accessed May 6, 2018).

(47) Jones, R. O.; Gunnarsson, O. The Density Functional Formalism, Its Applications and Prospects. *Rev. Mod. Phys.* **1989**, *61* (3), 689–746.

(48) Kresse, G.; Furthmüller, J. Efficiency of Ab-Initio Total Energy Calculations for Metals and Semiconductors Using a Plane-Wave Basis Set. *Comput. Mater. Sci.* **1996**, *6* (1), 15–50.

(49) Hammer, B.; Nørskov, J. K. Theoretical Surface Science and Catalysis—calculations and Concepts. In *Advances in Catalysis*; Impact of Surface Science on Catalysis; Academic Press, 2000; Vol. 45, pp 71–129.

(50) Klimeš, J.; Bowler, D. R.; Michaelides, A. Chemical Accuracy for the van Der Waals Density Functional. *J. Phys. Condens. Matter* **2010**, *22* (2), 022201.

(51) Klimeš, J.; Bowler, D. R.; Michaelides, A. Van Der Waals Density Functionals Applied to Solids. *Phys. Rev. B* **2011**, *83* (19), 195131.

(52) Bachelet, G. B.; Hamann, D. R.; Schlüter, M. Pseudopotentials That Work: From H to Pu. *Phys. Rev. B* **1982**, *26* (8), 4199–4228.

(53) Kresse, G.; Joubert, D. From Ultrasoft Pseudopotentials to the Projector Augmented-Wave Method. *Phys. Rev. B* **1999**, *59* (3), 1758.

(54) Vanderbilt, D. Soft Self-Consistent Pseudopotentials in a Generalized Eigenvalue Formalism. *Phys. Rev. B* **1990**, *41* (11), 7892–7895.

(55) Blöchl, P. E. Projector Augmented-Wave Method. *Phys. Rev. B* **1994**, *50* (24), 17953–17979.

(56) Panchakarla, L. S.; Subrahmanyam, K. S.; Saha, S. K.; Govindaraj, A.; Krishnamurthy, H. R.; Waghmare, U. V.; Rao, C. N. R. Synthesis, Structure, and Properties of Boron- and Nitrogen-Doped Graphene. *Adv. Mater.* **2009**, *21* (46), 4726–4730.

(57) Avramov, P. V.; Sakai, S.; Entani, S.; Matsumoto, Y.; Naramoto, H. Ab Initio LC-DFT Study of Graphene, Multilayer Graphenes and Graphite. *Chem. Phys. Lett.* **2011**, *508* (1), 86–89.

(58) (3) Van Der Waals Density Functionals for Graphene Layers and Graphite https://www.researchgate.net/publication/259715523_Van_Der_Waals_Density_Functionals_for_Graphene_Layers_and_Graphite (accessed May 7, 2018).

(59) Hammer, B.; Hansen, L. B.; Nørskov, J. K. Improved Adsorption Energetics within Density-Functional Theory Using Revised Perdew-Burke-Ernzerhof Functionals. *Phys. Rev. B* **1999**, *59* (11), 7413–7421.

(60) Krasheninnikov, A. V.; Lehtinen, P. O.; Foster, A. S.; Pyykkö, P.; Nieminen, R. M. Embedding Transition-Metal Atoms in Graphene: Structure, Bonding, and Magnetism. *Phys. Rev. Lett.* **2009**, *102* (12), 126807.

(61) Okazaki-Maeda, K.; Morikawa, Y.; Tanaka, S.; Kohyama, M. Structures of Pt Clusters on Graphene by First-Principles Calculations. *Surf. Sci.* **2010**, *604* (2), 144–154.

(62) Tang, Y.; Yang, Z.; Dai, X. Trapping of Metal Atoms in the Defects on Graphene. *J. Chem. Phys.* **2011**, *135* (22), 224704.

(63) Tang, Y.; Yang, Z.; Dai, X. A Theoretical Simulation on the Catalytic Oxidation of CO on Pt/Graphene. *Phys. Chem. Chem. Phys.* **2012**, *14* (48), 16566–16572.

(64) Tang, Y.; Yang, Z.; Dai, X. Noble Metals Induced Magnetic Properties of Graphene. *J. Magn. Magn. Mater.* **2011**, *323* (20), 2441–2447.

(65) Kennedy Kumfer. *In The Role of Soot in the Health Effects of Inhaled Airborne Particles, International Workshop on Combustion Generated Fine Carbonaceous Particles*; Scientific Publishing, 2009.

(66) *Contribution of Working Group I to the Fifth Assessment Report of the Intergovernmental Panel on Climate Change*; Stocker, T., Qin, D., Plattner, D., Tignor, M., Allen, M., Boschung, J., Nauels, A., Eds.; Cambridge University Press, 2013; Vol. IPCC (2013) Summary for policymakers.

(67) Howard, J. B. Carbon Addition and Oxidation Reactions in Heterogeneous Combustion and Soot Formation. *Symp. Int. Combust.* **1991**, *23* (1), 1107–1127.

(68) Bockhorn, H. *Soot Formation in Combustion: Mechanisms and Models*; Springer Science & Business Media, 2013; Vol. 59.

(69) Wang, H. Formation of Nascent Soot and Other Condensed-Phase Materials in Flames. *Proc. Combust. Inst.* **2011**, *33* (1), 41–67.

(70) Gross, E.; Liu, J. H.-C.; Toste, F. D.; Somorjai, G. A. Control of Selectivity in Heterogeneous Catalysis by Tuning Nanoparticle Properties and Reactor Residence Time. *Nat. Chem.* **2012**, *4* (11), 947–952.

(71) Wales, D. J.; Doye, J. P. K. Global Optimization by Basin-Hopping and the Lowest Energy Structures of Lennard-Jones Clusters Containing up to 110 Atoms. *J. Phys. Chem. A* **1997**, *101* (28), 5111–5116.

(72) Vander Wal, R. L.; Yezerets, A.; Currier, N. W.; Kim, D. H.; Wang, C. M. HRTEM Study of Diesel Soot Collected from Diesel Particulate Filters. *Carbon* **2007**, *45* (1), 70–77.

(73) Barone, A. C.; D'Alessio, A.; D'Anna, A. Morphological Characterization of the Early Process of Soot Formation by Atomic Force Microscopy. *Combust. Flame* **2003**, *132* (1), 181–187.

(74) Abid, A. D.; Heinz, N.; Tolmachoff, E. D.; Phares, D. J.; Campbell, C. S.; Wang, H. On Evolution of Particle Size Distribution Functions of Incipient Soot in Premixed Ethylene–oxygen–argon Flames. *Combust. Flame* **2008**, *154* (4), 775–788.

(75) Schenk, M.; Lieb, S.; Vieker, H.; Beyer, A.; Gölzhäuser, A.; Wang, H.; Kohse-Höinghaus, K. Imaging Nanocarbon Materials: Soot Particles in Flames Are Not Structurally Homogeneous. *ChemPhysChem* **2013**, *14* (14), 3248–3254.

(76) Schenk, M.; Lieb, S.; Vieker, H.; Beyer, A.; Gölzhäuser, A.; Wang, H.; Kohse-Höinghaus, K. Morphology of Nascent Soot in Ethylene Flames. *Proc. Combust. Inst.* **2015**, *35* (2), 1879–1886.

(77) Minutolo, P.; Commodo, M.; Santamaria, A.; De Falco, G.; D'Anna, A. Characterization of Flame-Generated 2-D Carbon Nano-Disks. *Carbon* **2014**, *68* (Supplement C), 138–148.

(78) Falco, G. D.; Commodo, M.; Minutolo, P.; D'Anna, A. Flame-Formed Carbon Nanoparticles: Morphology, Interaction Forces, and Hamaker Constant from AFM. *Aerosol Sci. Technol.* **2015**, *49* (5), 281–289.

(79) Rapacioli, M.; Calvo, F.; Spiegelman, F.; Joblin, C.; Wales, D. Stacked Clusters of Polycyclic Aromatic Hydrocarbon Molecules. *J. Phys. Chem. A* **2005**, *109* (11), 2487–2497.

(80) Totton, T. S.; Chakrabarti, D.; Misquitta, A. J.; Sander, M.; Wales, D. J.; Kraft, M. Modelling the Internal Structure of Nascent Soot Particles. *Combust. Flame* **2010**, *157* (5), 909–914.

(81) Pascazio, L.; Sirignano, M.; D'Anna, A. Simulating the Morphology of Clusters of Polycyclic Aromatic Hydrocarbons: The Influence of the Intermolecular Potential. *Combust. Flame* **2017**, *185*, 53–62.

(82) Richardson, N. V. Polyaromatic Hydrocarbons on Coinage Metal Surfaces. *Surf. Interface Sci. Solid-Gas Interfaces II* **2015**, 629–693.

(83) Maurer, R. J.; Ruiz, V. G.; Camarillo-Cisneros, J.; Liu, W.; Ferri, N.; Reuter, K.; Tkatchenko, A. Adsorption Structures and Energetics of Molecules on Metal Surfaces: Bridging Experiment and Theory. *Prog. Surf. Sci.* **2016**, *91* (2), 72–100.
(84) Lackinger, M.; Griessl, S.; Heckl, W. M.; Hietschold, M. Coronene on Ag (111) Investigated by LEED and STM in UHV. *J. Phys. Chem. B* **2002**, *106* (17), 4482–4485.
(85) Lackinger, M.; Griessl, S.; Heckl, W. M.; Hietschold, M. STM and STS of Coronene on HOPG (0001) in UHV-Adsorption of the Smallest Possible Graphite Flakes on Graphite. *Anal. Bioanal. Chem.* **2002**, *374* (4), 685–687.
(86) Yoshimoto, S.; Narita, R.; Wakisaka, M.; Itaya, K. The Structure of a Coronene Adlayer Formed in a Benzene Solution: Studies by in Situ STM and Ex Situ LEED. *J. Electroanal. Chem.* **2002**, *532* (1), 331–335.
(87) Griessl, S. J. H.; Lackinger, M.; Jamitzky, F.; Markert, T.; Hietschold, M.; Heckl, W. M. Incorporation and Manipulation of Coronene in an Organic Template Structure. *Langmuir* **2004**, *20* (21), 9403–9407.
(88) Walzer, K.; Sternberg, M.; Hietschold, M. Formation and Characterization of Coronene Monolayers on HOPG (0001) and MoS 2 (0001): A Combined STM/STS and Tight-Binding Study. *Surf. Sci.* **1998**, *415* (3), 376–384.
(89) Huempfner, T.; Sojka, F.; Forker, R.; Fritz, T. Growth of Coronene on (100)- and (111)-Surfaces of Fcc-Crystals. *Surf. Sci.* **2015**, *639*, 80–88.
(90) Forker, R.; Peuker, J.; Meissner, M.; Sojka, F.; Ueba, T.; Yamada, T.; Kato, H. S.; Munakata, T.; Fritz, T. The Complex Polymorphism and Thermodynamic Behavior of a Seemingly Simple System: Naphthalene on Cu (111). *Langmuir* **2014**, *30* (47), 14163–14170.
(91) Janiak, C. A Critical Account on Π–π Stacking in Metal Complexes with Aromatic Nitrogen-Containing Ligands. *J. Chem. Soc. Dalton Trans.* **2000**, No. 21, 3885–3896.
(92) Obolensky, O.; Semenikhina, V.; Solov'Yov, A.; Greiner, W. Interplay of Electrostatic and van Der Waals Forces in Coronene Dimer. *Int. J. Quantum Chem.* **2007**, *107* (6), 1335–1343.
(93) Martínez-Blanco, J.; Mascaraque, A.; Dedkov, Y. S.; Horn, K. Ge(001) As a Template for Long-Range Assembly of π-Stacked Coronene Rows. *Langmuir* **2012**, *28* (8), 3840–3844.
(94) Kresse, G.; Hafner, J. Ab Initio Molecular-Dynamics Simulation of the Liquid-Metal–amorphous-Semiconductor Transition in Germanium. *Phys. Rev. B* **1994**, *49* (20), 14251.
(95) Vander Wal, R. L.; Tomasek, A. J. Soot Oxidation: Dependence upon Initial Nanostructure. *Combust. Flame* **2003**, *134* (1), 1–9.
(96) Violi, A. Modeling of Soot Particle Inception in Aromatic and Aliphatic Premixed Flames. *Combust. Flame* **2004**, *139* (4), 279–287.
(97) Bell, A. T. The Impact of Nanoscience on Heterogeneous Catalysis. *Science* **2003**, *299* (5613), 1688–1691.
(98) Zhang, J.; Sasaki, K.; Sutter, E.; Adzic, R. R. Stabilization of Platinum Oxygen-Reduction Electrocatalysts Using Gold Clusters. *Science* **2007**, *315* (5809), 220–222.
(99) Vajda, S.; Pellin, M. J.; Greeley, J. P.; Marshall, C. L.; Curtiss, L. A.; Ballentine, G. A.; Elam, J. W.; Catillon-Mucherie, S.; Redfern, P. C.; Mehmood, F.; et al. Subnanometre Platinum Clusters as Highly Active and Selective Catalysts for the Oxidative Dehydrogenation of Propane. *Nat. Mater.* **2009**, *8* (3), 213–216.
(100) Zang, W.; Li, G.; Wang, L.; Zhang, X. Catalytic Hydrogenation by Noble-Metal Nanocrystals with Well-Defined Facets: A Review. *Catal. Sci. Technol.* **2015**, *5* (5), 2532–2553.
(101) Fan, Z.; Zhang, H. Template Synthesis of Noble Metal Nanocrystals with Unusual Crystal Structures and Their Catalytic Applications. *Acc. Chem. Res.* **2016**, *49* (12), 2841–2850.
(102) J, H. G.; G, D. M.; A, C. R. C. *Modern Developments In Catalysis*; World Scientific, 2016.
(103) Wang, Y.; Arandiyan, H.; Scott, J.; Bagheri, A.; Dai, H.; Amal, R. Recent Advances in Ordered Meso/Macroporous Metal Oxides for Heterogeneous Catalysis: A Review. *J. Mater. Chem. A* **2017**, *5* (19), 8825–8846.
(104) Qiao, B.; Wang, A.; Yang, X.; Allard, L. F.; Jiang, Z.; Cui, Y.; Liu, J.; Li, J.; Zhang, T. Single-Atom Catalysis of CO Oxidation Using Pt_1/FeO_X. *Nat. Chem.* **2011**, *3* (8), 634.
(105) Sun, S.; Zhang, G.; Gauquelin, N.; Chen, N.; Zhou, J.; Yang, S.; Chen, W.; Meng, X.; Geng, D.; Banis, M. N.; et al. Single-Atom Catalysis Using Pt/Graphene Achieved through Atomic Layer Deposition. *Sci. Rep.* **2013**, *3*.
(106) Yang, X.-F.; Wang, A.; Qiao, B.; Li, J.; Liu, J.; Zhang, T. Single-Atom Catalysts: A New Frontier in Heterogeneous Catalysis. *Acc. Chem. Res.* **2013**, *46* (8), 1740–1748.
(107) Wei, H.; Liu, X.; Wang, A.; Zhang, L.; Qiao, B.; Yang, X.; Huang, Y.; Miao, S.; Liu, J.; Zhang, T. FeO_x-Supported Platinum Single-Atom and Pseudo-Single-Atom Catalysts for Chemoselective Hydrogenation of Functionalized Nitroarenes. *Nat. Commun.* **2014**, *5*, 5634.

(108) Kim, Y.-T.; Ohshima, K.; Higashimine, K.; Uruga, T.; Takata, M.; Suematsu, H.; Mitani, T. Fine Size Control of Platinum on Carbon Nanotubes: From Single Atoms to Clusters. *Angew. Chem.* **2006**, *118* (3), 421–425.

(109) Thomas, J. M.; Saghi, Z.; Gai, P. L. Can a Single Atom Serve as the Active Site in Some Heterogeneous Catalysts? *Top. Catal.* **2011**, *54* (10–12), 588–594.

(110) Song, E. H.; Wen, Z.; Jiang, Q. CO Catalytic Oxidation on Copper-Embedded Graphene. *J. Phys. Chem. C* **2011**, *115* (9), 3678–3683.

(111) Li, Y.; Zhou, Z.; Yu, G.; Chen, W.; Chen, Z. CO Catalytic Oxidation on Iron-Embedded Graphene: Computational Quest for Low-Cost Nanocatalysts. *J. Phys. Chem. C* **2010**, *114* (14), 6250–6254.

(112) Lu, Y.-H.; Zhou, M.; Zhang, C.; Feng, Y.-P. Metal-Embedded Graphene: A Possible Catalyst with High Activity. *J. Phys. Chem. C* **2009**, *113* (47), 20156–20160.

(113) Kim, G.; Jhi, S.-H. Carbon Monoxide-Tolerant Platinum Nanoparticle Catalysts on Defect-Engineered Graphene. *ACS Nano* **2011**, *5* (2), 805–810.

(114) Zhou, M.; Zhang, A. H.; Dai, Z. X.; Zhang, C.; Feng, Y. P. Greatly Enhanced Adsorption and Catalytic Activity of Au and Pt Clusters on Defective Graphene. *J. Chem. Phys.* **2010**, *132* (19), 194704.

(115) Yoo, E.; Okata, T.; Akita, T.; Kohyama, M.; Nakamura, J.; Honma, I. Enhanced Electrocatalytic Activity of Pt Subnanoclusters on Graphene Nanosheet Surface. *Nano Lett.* **2009**, *9* (6), 2255–2259.

(116) Yoo, E.; Okada, T.; Akita, T.; Kohyama, M.; Honma, I.; Nakamura, J. Sub-Nano-Pt Cluster Supported on Graphene Nanosheets for CO Tolerant Catalysts in Polymer Electrolyte Fuel Cells. *J. Power Sources* **2011**, *196* (1), 110–115.

(117) Kou, R.; Shao, Y.; Mei, D.; Nie, Z.; Wang, D.; Wang, C.; Viswanathan, V. V.; Park, S.; Aksay, I. A.; Lin, Y.; et al. Stabilization of Electrocatalytic Metal Nanoparticles at Metal−Metal Oxide−Graphene Triple Junction Points. *J. Am. Chem. Soc.* **2011**, *133* (8), 2541–2547.

(118) Uzun, A.; Ortalan, V.; Browning, N. D.; Gates, B. C. A Site-Isolated Mononuclear Iridium Complex Catalyst Supported on MgO: Characterization by Spectroscopy and Aberration-Corrected Scanning Transmission Electron Microscopy. *J. Catal.* **2010**, *269* (2), 318–328.

(119) Uzun, A.; Ortalan, V.; Hao, Y.; Browning, N. D.; Gates, B. C. Nanoclusters of Gold on a High-Area Support: Almost Uniform Nanoclusters Imaged by Scanning Transmission Electron Microscopy. *ACS Nano* **2009**, *3* (11), 3691–3695.

(120) Kresse, G.; Furthmüller, J. Efficient Iterative Schemes for Ab Initio Total-Energy Calculations Using a Plane-Wave Basis Set. *Phys. Rev. B* **1996**, *54* (16), 11169.

(121) Momma, K.; Izumi, F. VESTA 3 for Three-Dimensional Visualization of Crystal, Volumetric and Morphology Data. *J. Appl. Crystallogr.* **2011**, *44* (6), 1272–1276.

(122) Henkelman, G.; Jónsson, H. Improved Tangent Estimate in the Nudged Elastic Band Method for Finding Minimum Energy Paths and Saddle Points. *J. Chem. Phys.* **2000**, *113* (22), 9978–9985.

(123) Henkelman, G.; Uberuaga, B. P.; Jónsson, H. A Climbing Image Nudged Elastic Band Method for Finding Saddle Points and Minimum Energy Paths. *J. Chem. Phys.* **2000**, *113* (22), 9901–9904.

(124) Sheppard, D.; Terrell, R.; Henkelman, G. Optimization Methods for Finding Minimum Energy Paths. *J. Chem. Phys.* **2008**, *128* (13), 134106.

(125) Sheppard, D.; Henkelman, G. Paths to Which the Nudged Elastic Band Converges. *J. Comput. Chem.* **2011**, *32* (8), 1769–1771.

(126) Sheppard, D.; Xiao, P.; Chemelewski, W.; Johnson, D. D.; Henkelman, G. A Generalized Solid-State Nudged Elastic Band Method. *J. Chem. Phys.* **2012**, *136* (7), 074103.

(127) Tison, Y.; Lagoute, J.; Repain, V.; Chacon, C.; Girard, Y.; Rousset, S.; Joucken, F.; Sharma, D.; Henrard, L.; Amara, H.; et al. Electronic Interaction between Nitrogen Atoms in Doped Graphene. *ACS Nano* **2015**, *9* (1), 670–678.

(128) Joucken, F.; Tison, Y.; Lagoute, J.; Dumont, J.; Cabosart, D.; Zheng, B.; Repain, V.; Chacon, C.; Girard, Y.; Botello-Méndez, A. R.; et al. Localized State and Charge Transfer in Nitrogen-Doped Graphene. *Phys. Rev. B* **2012**, *85* (16), 161408.

(129) Zhao, L.; He, R.; Rim, K. T.; Schiros, T.; Kim, K. S.; Zhou, H.; Gutiérrez, C.; Chockalingam, S. P.; Arguello, C. J.; Pálová, L.; et al. Visualizing Individual Nitrogen Dopants in Monolayer Graphene. *Science* **2011**, *333* (6045), 999–1003.

(130) Üzengi Aktürk, O.; Tomak, M. ${\text{Au}}_{n}{\text{Pt}}_{n}$. *Phys. Rev. B* **2009**, *80* (8), 085417.

(131) Chi, D. H.; Cuong, N. T.; Tuan, N. A.; Kim, Y.-T.; Bao, H. T.; Mitani, T.; Ozaki, T.; Nagao, H. Electronic Structures of Pt Clusters Adsorbed on (5,5) Single Wall Carbon Nanotube. *Chem. Phys. Lett.* **2006**, *432* (1), 213–217.

(132) Ganji, M. D.; Sharifi, N.; Ardjmand, M.; Ahangari, M. G. Pt-Decorated Graphene as Superior Media for H2S Adsorption: A First-Principles Study. *Appl. Surf. Sci.* **2012**, *261* (Supplement C), 697–704.

(133) Muhich, C. L.; Westcott, J. Y.; Morris, T. C.; Weimer, A. W.; Musgrave, C. B. The Effect of N and B Doping on Graphene and the Adsorption and Migration Behavior of Pt Atoms. *J. Phys. Chem. C* **2013**, *117* (20), 10523–10535.

(134) Blonski, P.; Hafner, J. Geometric and Magnetic Properties of Pt Clusters Supported on Graphene: Relativistic Density-Functional Calculations. *J. Chem. Phys.* **2011**, *134* (15), 12.

(135) Fampiou, I.; Ramasubramaniam, A. Binding of Pt Nanoclusters to Point Defects in Graphene: Adsorption, Morphology, and Electronic Structure. *J. Phys. Chem. C* **2012**, *116* (11), 6543–6555.

(136) Tang, Y.; Liu, Z.; Chen, W.; Shen, Z.; Li, C.; Dai, X. Theoretical Study on the Removal of Adsorbed Sulfur on Pt Anchored Graphene Surfaces. *Int. J. Hydrog. Energy* **2015**, *40* (21), 6942–6949.

(137) Błoński, P.; Hafner, J. Magnetic Anisotropy of Heteronuclear Dimers in the Gas Phase and Supported on Graphene: Relativistic Density-Functional Calculations. *J. Phys. Condens. Matter* **2014**, *26* (14), 146002.

(138) Hammer, B.; Nielsen, O. H.; Nrskov, J. K. Structure Sensitivity in Adsorption: CO Interaction with Stepped and Reconstructed Pt Surfaces. *Catal. Lett.* **1997**, *46* (1–2), 31–35.

(139) Mostafa, S.; Behafarid, F.; Croy, J. R.; Ono, L. K.; Li, L.; Yang, J. C.; Frenkel, A. I.; Cuenya, B. R. Shape-Dependent Catalytic Properties of Pt Nanoparticles. *J. Am. Chem. Soc.* **2010**, *132* (44), 15714–15719.

(140) Kale, M. J.; Christopher, P. Utilizing Quantitative in Situ FTIR Spectroscopy To Identify Well-Coordinated Pt Atoms as the Active Site for CO Oxidation on Al2O3-Supported Pt Catalysts. *ACS Catal.* **2016**, *6* (8), 5599–5609.

(141) Tang, Y.; Yang, Z.; Dai, X.; Ma, D.; Fu, Z. Formation, Stabilities, and Electronic and Catalytic Performance of Platinum Catalyst Supported on Non-Metal-Doped Graphene. *J. Phys. Chem. C* **2013**, *117* (10), 5258–5268.

(142) Holme, T.; Zhou, Y.; Pasquarelli, R.; O'Hayre, R. First Principles Study of Doped Carbon Supports for Enhanced Platinum Catalysts. *Phys. Chem. Chem. Phys.* **2010**, *12* (32), 9461–9468.

(143) Cheng, N.; Stambula, S.; Wang, D.; Banis, M. N.; Liu, J.; Riese, A.; Xiao, B.; Li, R.; Sham, T.-K.; Liu, L.-M.; et al. Platinum Single-Atom and Cluster Catalysis of the Hydrogen Evolution Reaction. *Nat. Commun.* **2016**, *7*.

(144) Guo, D.; Shibuya, R.; Akiba, C.; Saji, S.; Kondo, T.; Nakamura, J. Active Sites of Nitrogen-Doped Carbon Materials for Oxygen Reduction Reaction Clarified Using Model Catalysts. *Science* **2016**, *351* (6271), 361–365.

(145) Lai, L.; R. Potts, J.; Zhan, D.; Wang, L.; Kok Poh, C.; Tang, C.; Gong, H.; Shen, Z.; Lin, J.; S. Ruoff, R. Exploration of the Active Center Structure of Nitrogen-Doped Graphene-Based Catalysts for Oxygen Reduction Reaction. *Energy Environ. Sci.* **2012**, *5* (7), 7936–7942.

(146) Luo, Z.; Lim, S.; Tian, Z.; Shang, J.; Lai, L.; MacDonald, B.; Fu, C.; Shen, Z.; Yu, T.; Lin, J. Pyridinic N Doped Graphene : Synthesis, Electronic Structure, and Electrocatalytic Property. *J. Mater. Chem.* **2011**, *21* (22), 8038–8044.

(147) Groves, M. N.; Chan, A. S. W.; Malardier-Jugroot, C.; Jugroot, M. Improving Platinum Catalyst Binding Energy to Graphene through Nitrogen Doping. *Chem. Phys. Lett.* **2009**, *481* (4–6), 214–219.

(148) Cheng, N.; Stambula, S.; Wang, D.; Banis, M. N.; Liu, J.; Riese, A.; Xiao, B.; Li, R.; Sham, T.-K.; Liu, L.-M.; et al. Platinum Single-Atom and Cluster Catalysis of the Hydrogen Evolution Reaction. *Nat. Commun.* **2016**, *7*.

(149) Zou, X.; Zhang, Y. Noble Metal-Free Hydrogen Evolution Catalysts for Water Splitting. *Chem. Soc. Rev.* **2015**, *44* (15), 5148–5180.

(150) Lee, Y.; Lee, S.; Hwang, Y.; Chung, Y.-C. Modulating Magnetic Characteristics of Pt Embedded Graphene by Gas Adsorption (N2, O2, NO2, SO2). *Appl. Surf. Sci.* **2014**, *289* (Supplement C), 445–449.

(151) Brix, P.; Herzberg, G. The Dissociation Energy of Oxygen. *J. Chem. Phys.* **1953**, *21* (12), 2240–2240.

(152) Du, X.; Skachko, I.; Barker, A.; Andrei, E. Y. Approaching Ballistic Transport in Suspended Graphene. *Nat. Nanotechnol.* **2008**, *3* (8), 491–495.

(153) Bolotin, K. I.; Sikes, K. J.; Hone, J.; Stormer, H. L.; Kim, P. Temperature-Dependent Transport in Suspended Graphene. *Phys. Rev. Lett.* **2008**, *101* (9), 096802.

(154) Castro Neto, A. H.; Guinea, F.; Peres, N. M. R.; Novoselov, K. S.; Geim, A. K. The Electronic Properties of Graphene. *Rev. Mod. Phys.* **2009**, *81* (1), 109–162.

(155) Hu, G.; Xu, C.; Sun, Z.; Wang, S.; Cheng, H.-M.; Li, F.; Ren, W. 3D Graphene-Foam–Reduced-Graphene-Oxide Hybrid Nested Hierarchical Networks for High-Performance Li–S Batteries. *Adv. Mater.* **2016**, *28* (8), 1603–1609.

(156) Georgakilas, V.; Tiwari, J. N.; Kemp, K. C.; Perman, J. A.; Bourlinos, A. B.; Kim, K. S.; Zboril, R. Noncovalent Functionalization of Graphene and Graphene Oxide for Energy Materials, Biosensing, Catalytic, and Biomedical Applications. *Chem. Rev.* **2016**, *116* (9), 5464–5519.

(157) Jiang, W.; Xin, H.; Li, W. Microcellular 3D Graphene Foam via Chemical Vapor Deposition of Electroless Plated Nickel Foam Templates. *Mater. Lett.* **2016**, *162*, 105–109.

(158) Li, C.; Shi, G. Three-Dimensional Graphene Architectures. *Nanoscale* **2012**, *4* (18), 5549–5563.

(159) Chen, W.; Yan, L. In Situ Self-Assembly of Mild Chemical Reduction Graphene for Three-Dimensional Architectures. *Nanoscale* **2011**, *3* (8), 3132–3137.

(160) Cao, X.; Shi, Y.; Shi, W.; Lu, G.; Huang, X.; Yan, Q.; Zhang, Q.; Zhang, H. Preparation of Novel 3D Graphene Networks for Supercapacitor Applications. *Small* **2011**, *7* (22), 3163–3168.

(161) Yuan, K.; Xu, Y.; Uihlein, J.; Brunklaus, G.; Shi, L.; Heiderhoff, R.; Que, M.; Forster, M.; Chassé, T.; Pichler, T.; et al. Straightforward Generation of Pillared, Microporous Graphene Frameworks for Use in Supercapacitors. *Adv. Mater.* **2015**, *27* (42), 6714–6721.

(162) Xiao, X.; Beechem, T. E.; Brumbach, M. T.; Lambert, T. N.; Davis, D. J.; Michael, J. R.; Washburn, C. M.; Wang, J.; Brozik, S. M.; Wheeler, D. R.; et al. Lithographically Defined Three-Dimensional Graphene Structures. *ACS Nano* **2012**, *6* (4), 3573–3579.

(163) Ito, Y.; Tanabe, Y.; Qiu, H.-J.; Sugawara, K.; Heguri, S.; Tu, N. H.; Huynh, K. K.; Fujita, T.; Takahashi, T.; Tanigaki, K.; et al. High-Quality Three-Dimensional Nanoporous Graphene. *Angew. Chem.* **2014**, *126* (19), 4922–4926.

(164) Dong, X.; Ma, Y.; Zhu, G.; Huang, Y.; Wang, J.; Chan-Park, M. B.; Wang, L.; Huang, W.; Chen, P. Synthesis of Graphene–carbon Nanotube Hybrid Foam and Its Use as a Novel Three-Dimensional Electrode for Electrochemical Sensing. *J. Mater. Chem.* **2012**, *22* (33), 17044.

(165) Ning, J.; Xu, X.; Liu, C.; Fan, D. L. Three-Dimensional Multilevel Porous Thin Graphite Nanosuperstructures for $Ni(OH)_2$ -Based Energy Storage Devices. *J Mater Chem A* **2014**, *2* (38), 15768–15773.

(166) Singh, E.; Chen, Z.; Houshmand, F.; Ren, W.; Peles, Y.; Cheng, H.-M.; Koratkar, N. Superhydrophobic Graphene Foams. *Small* **2013**, *9* (1), 75–80.

(167) Herzig, E. M.; White, K. A.; Schofield, A. B.; Poon, W. C. K.; Clegg, P. S. Bicontinuous Emulsions Stabilized Solely by Colloidal Particles. *Nat. Mater.* **2007**, *6* (12), 966–971.

(168) Witt, J. A.; Mumm, D. R.; Mohraz, A. Bijel Reinforcement by Droplet Bridging: A Route to Bicontinuous Materials with Large Domains. *Soft Matter* **2013**, *9* (29), 6773–6780.

(169) Nishikawa, Y.; Jinnai, H.; Koga, T.; Hashimoto, T.; Hyde, S. T. Measurements of Interfacial Curvatures of Bicontinuous Structure from Three-Dimensional Digital Images. 1. A Parallel Surface Method. *Langmuir* **1998**, *14* (5), 1242–1249.

(170) Cates, M. E.; Clegg, P. S. Bijels: A New Class of Soft Materials. *Soft Matter* **2008**, *4*, 2132–2138.

(171) Lee, M. N.; Mohraz, A. Bicontinuous Macroporous Materials from Bijel Templates. *Adv. Mater.* **2010**, *22* (43), 4836–4841.

(172) Lee, M. N.; Thijssen, J. H. J.; Witt, J. A.; Clegg, P. S.; Mohraz, A. Making a Robust Interfacial Scaffold: Bijel Rheology and Its Link to Processability. *Adv. Funct. Mater.* **2013**, *23* (4), 417–423.

(173) Chen, H.-Y.; Kwon, Y.; Thornton, K. Multifunctionality of Three-Dimensional Self-Assembled Composite Structure. *Scr. Mater.* **2009**, *61* (1), 52–55.

(174) A. Witt, J.; R. Mumm, D.; Mohraz, A. Microstructural Tunability of Co-Continuous Bijel-Derived Electrodes to Provide High Energy and Power Densities. *J. Mater. Chem. A* **2016**, *4* (3), 1000–1007.

(175) Reina, A.; Jia, X.; Ho, J.; Nezich, D.; Son, H.; Bulovic, V.; Dresselhaus, M. S.; Kong, J. Large Area, Few-Layer Graphene Films on Arbitrary Substrates by Chemical Vapor Deposition. *Nano Lett.* **2009**, *9* (1), 30–35.

(176) Thiele, S.; Reina, A.; Healey, P.; Kedzierski, J.; Wyatt, P.; Hsu, P.-L.; Keast, C.; Schaefer, J.; Kong, J. Engineering Polycrystalline Ni Films to Improve Thickness Uniformity of the Chemical-Vapor-Deposition-Grown Graphene Films. *Nanotechnology* **2010**, *21* (1), 015601.

(177) De Arco, L. G.; Yi Zhang; Kumar, A.; Chongwu Zhou. Synthesis, Transfer, and Devices of Single- and Few-Layer Graphene by Chemical Vapor Deposition. *IEEE Trans. Nanotechnol.* **2009**, *8* (2), 135–138.

(178) Blyth, R. I. .; Buqa, H.; Netzer, F. .; Ramsey, M. .; Besenhard, J. .; Golob, P.; Winter, M. XPS Studies of Graphite Electrode Materials for Lithium Ion Batteries. *Appl. Surf. Sci.* **2000**, *167* (1–2), 99–106.

(179) Das, A.; Chakraborty, B.; Sood, A. K. Raman Spectroscopy of Graphene on Different Substrates and Influence of Defects. *Bull. Mater. Sci.* **2008**, *31* (3), 579–584.

(180) Ferrari, A. C. Raman Spectroscopy of Graphene and Graphite: Disorder, Electron–phonon Coupling, Doping and Nonadiabatic Effects. *Solid State Commun.* **2007**, *143* (1–2), 47–57.

(181) Marchand, A.; Lespade, P.; Couzi, M. Characterization of Carbon-Carbon Composites by Raman Microprobe. *15th Bienn. Conf Carbon* **1981**, 282–283.
(182) Mogera, U.; Dhanya, R.; Pujar, R.; Narayana, C.; Kulkarni, G. U. Highly Decoupled Graphene Multilayers: Turbostraticity at Its Best. *J. Phys. Chem. Lett.* **2015**, *6* (21), 4437–4443.
(183) Dahal, A.; Batzill, M. Graphene–nickel Interfaces: A Review. *Nanoscale* **2014**, *6* (5), 2548–2562.
(184) Kim, K.; Coh, S.; Tan, L. Z.; Regan, W.; Yuk, J. M.; Chatterjee, E.; Crommie, M. F.; Cohen, M. L.; Louie, S. G.; Zettl, A. Raman Spectroscopy Study of Rotated Double-Layer Graphene: Misorientation-Angle Dependence of Electronic Structure. *Phys. Rev. Lett.* **2012**, *108* (24), 246103.
(185) Li, X.; Cai, W.; An, J.; Kim, S.; Nah, J.; Yang, D.; Piner, R.; Velamakanni, A.; Jung, I.; Tutuc, E.; et al. Large-Area Synthesis of High-Quality and Uniform Graphene Films on Copper Foils. *Science* **2009**, *324* (5932), 1312–1314.
(186) Yeh, C.-H.; Lin, Y.-C.; Nayak, P. K.; Lu, C.-C.; Liu, Z.; Suenaga, K.; Chiu, P.-W. Probing Interlayer Coupling in Twisted Single-Crystal Bilayer Graphene by Raman Spectroscopy. *J. Raman Spectrosc.* **2014**, *45* (10), 912–917.
(187) Wu, J.-B.; Wang, H.; Li, X.-L.; Peng, H.; Tan, P.-H. Raman Spectroscopic Characterization of Stacking Configuration and Interlayer Coupling of Twisted Multilayer Graphene Grown by Chemical Vapor Deposition. *Carbon* **2016**, *110* (Supplement C), 225–231.
(188) Zhang, Y.; Gao, T.; Xie, S.; Dai, B.; Fu, L.; Gao, Y.; Chen, Y.; Liu, M.; Liu, Z. Different Growth Behaviors of Ambient Pressure Chemical Vapor Deposition Graphene on Ni(111) and Ni Films: A Scanning Tunneling Microscopy Study. *Nano Res.* **2012**, *5* (6), 402–411.
(189) Shelton, J. C.; Patil, H. R.; Blakely, J. M. Equilibrium Segregation of Carbon to a Nickel (111) Surface: A Surface Phase Transition. *Surf. Sci.* **1974**, *43* (2), 493–520.
(190) Choi, B. G.; Yang, M.; Hong, W. H.; Choi, J. W.; Huh, Y. S. 3D Macroporous Graphene Frameworks for Supercapacitors with High Energy and Power Densities. *ACS Nano* **2012**, *6* (5), 4020–4028.
(191) Dimitrakakis, G. K.; Tylianakis, E.; Froudakis, G. E. Pillared Graphene: A New 3-D Network Nanostructure for Enhanced Hydrogen Storage. *Nano Lett.* **2008**, *8* (10), 3166–3170.
(192) He, X.; Zhang, H.; Zhang, H.; Li, X.; Xiao, N.; Qiu, J. Direct Synthesis of 3D Hollow Porous Graphene Balls from Coal Tar Pitch for High Performance Supercapacitors. *J Mater Chem A* **2014**, *2* (46), 19633–19640.
(193) Wang, L.; Sofer, Z.; Ambrosi, A.; Šimek, P.; Pumera, M. 3D-Graphene for Electrocatalysis of Oxygen Reduction Reaction: Increasing Number of Layers Increases the Catalytic Effect. *Electrochem. Commun.* **2014**, *46*, 148–151.
(194) Thorson, T. J.; Botvinick, E. L.; Mohraz, A. Composite Bijel-Templated Hydrogels for Cell Delivery. *ACS Biomater. Sci. Eng.* **2018**, *4* (2), 587–594.
(195) Hu, H.; Zhao, Z.; Wan, W.; Gogotsi, Y.; Qiu, J. Ultralight and Highly Compressible Graphene Aerogels. *Adv. Mater.* **2013**, *25* (15), 2219–2223.
(196) Sun, H.; Xu, Z.; Gao, C. Multifunctional, Ultra-Flyweight, Synergistically Assembled Carbon Aerogels. *Adv. Mater.* **2013**, *25* (18), 2554–2560.
(197) Li, Y.; Chen, J.; Huang, L.; Li, C.; Hong, J.-D.; Shi, G. Highly Compressible Macroporous Graphene Monoliths via an Improved Hydrothermal Process. *Adv. Mater.* **2014**, *26* (28), 4789–4793.
(198) Nieto, A.; Boesl, B.; Agarwal, A. Multi-Scale Intrinsic Deformation Mechanisms of 3D Graphene Foam. *Carbon* **2015**, *85*, 299–308.
(199) Zhang, Q.; Zhang, F.; Medarametla, S. P.; Li, H.; Zhou, C.; Lin, D. 3D Printing of Graphene Aerogels. *Small* **2016**, *12* (13), 1702–1708.
(200) Lv, L.; Zhang, P.; Cheng, H.; Zhao, Y.; Zhang, Z.; Shi, G.; Qu, L. Solution-Processed Ultraelastic and Strong Air-Bubbled Graphene Foams. *Small* **2016**, *12* (24), 3229–3234.